Title: A multiparametric anti-aging CRISPR screen uncovers a role for BAF in protein synthesis regulation

Author list:

Sophia Y. Breusegem[1,6], Jack Houghton[1,7], Raquel Romero-Bueno[2#], Adrián Fragoso-Luna[2#], Katherine A. Kentistou[3], Ken K. Ong[3], Anne F. J. Janssen[1,8], Nicholas A. Bright[1], Christian G. Riedel[4], John R. B. Perry[3,5], Peter Askjaer[2] and Delphine Larrieu[1,9*]

Affiliations:

[1]Cambridge Institute for Medical Research, University of Cambridge, Cambridge Biomedical Campus, Keith Peters Building, Hills Road, Cambridge, CB2 0XY, UK.

[2] Centro Andaluz de Biología del Desarrollo (CABD), Consejo Superior de Investigaciones Científicas-Universidad Pablo de Olavide-Junta de Andalucía, 41013 Seville, Spain.

[3] MRC Epidemiology Unit, University of Cambridge School of Clinical Medicine, Institute of Metabolic Science, Cambridge, CB2 0QQ, UK.

[4] Karolinska Institutet, Blickagången 16, 141 57 Huddinge, Sweden.

[5]Metabolic Research Laboratory, Wellcome-MRC Institute of Metabolic Science, University of Cambridge School of Clinical Medicine, Cambridge CB2 0QQ, UK

Present addresses:

[6]Sophia Y. Breusegem: MRC toxicology Unit, University of Cambridge, Tennis Court Road, Cambridge CB2 1QR, UK

[7]Jack Houghton: Imperial College London, Exhibition Road, South Kensington, London SW7 2AZ, UK

[8]Anne F. J. Janssen: Institute for Molecules and Materials, Radboud University, Heyendaalseweg 135, 6525 AJ, Nijmegen, The Netherlands

[9]Delphine Larrieu: Altos Labs, Cambridge Institute of Science, Cambridge CB21 6GP, UK

[#]These authors contributed equally

*Corresponding author. Email: dlarrieu@altoslabs.com

ABSTRACT

Progeria syndromes are very rare, incurable premature aging conditions recapitulating most aging features. Here, we report a whole genome, multiparametric CRISPR screen, identifying 43 genes that can rescue multiple cellular phenotypes associated with progeria. We implement the screen in fibroblasts from Néstor-Guillermo Progeria Syndrome male patients, carrying a homozygous A12T mutation in BAF. The hits are enriched for genes involved in protein synthesis, protein and RNA transport and osteoclast formation and are validated in a whole-organism *Caenorhabditis elegans* model. We further confirm that BAF A12T can disrupt protein synthesis rate and fidelity, which could contribute to premature aging in patients. This work highlights the power of multiparametric genome-wide suppressor screens to identify genes enhancing cellular resilience in premature aging and provide insights into the biology underlying progeria-associated cellular dysfunction.

INTRODUCTION

Premature aging syndromes (progerias) are very rare conditions that recapitulate many aspects of physiological aging, causing symptoms such as alopecia, lipodystrophy, cardiovascular dysfunction, and bone dysfunction well before the expected age of onset. Many progeria syndromes are caused by mutations in nuclear envelope (NE) associated proteins. For example, the classic Hutchinson-Gilford progeria syndrome (HGPS) is caused by mutations in *LMNA* encoding for the nuclear lamina proteins lamin A and C (*1*, *2*). A more recently described progeria, Néstor-Guillermo progeria syndrome (NGPS), is caused by a recessive alanine to threonine amino acid substitution at position 12 (p.Ala12Thr) in the *BANF1* gene, encoding the 10 KDa protein barrier-to-autointegration factor (BAF) (*3*, *4*). BAF forms dimers that bind to DNA (*5*, *6*), lamin proteins as well as LEM-domain containing proteins of the inner nuclear membrane including emerin (*7*, *8*). Through these interactions, BAF exerts critical functions

including reformation of the NE after mitosis (*9*, *10*) and NE rupture repair (*11*). NGPS patients suffer from multiple aging-associated pathologies, such as alopecia and lipodystrophy, as well as osteoarthritis and joint stiffness. However, the most severe phenotype affecting their quality of life is bone dysfunction, with osteoporosis and dramatic skeletal deformation (*3, 4*). NGPS patients have an increased life expectancy compared to HGPS, probably due to the absence of cardiovascular dysfunction, the main cause of death in HGPS (*12, 13*).

NGPS remains poorly characterized compared to HGPS, and insights into the molecular mechanisms behind the disease have only recently started to emerge (*14-16*). Therefore, with the aim of identifying genes and pathways relevant to NGPS, as well as potential targets for therapeutic avenues in the disease, we carried out a whole genome CRISPR/Cas9 arrayed microscopy screen in patient-derived NGPS cells. We assessed the impact of deleting each of the ~20,000 human genes on four specific cellular NGPS phenotypes simultaneously, to identify "rescue" genes acting across several phenotypes. Through this approach, we identified 43 genes enriched in pathways including protein synthesis and bone cell development, that improve NGPS cellular phenotypes.

RESULTS

NGPS fibroblasts show distinct phenotypes compared to HGPS

Fibroblasts from HGPS patients have been extensively studied and characterized. The best-established phenotypes in these cells include NE blebs and invaginations, loss of heterochromatin, downregulation of lamin B1, nucleocytoplasmic transport defects and accumulation of DNA damage foci (*17-22*). To establish whether NGPS cells might share similar phenotypes, we obtained immortalized fibroblasts from two of the three so far identified NGPS patients (NGPS1 and NGPS2 – both males) and age-matched immortalized fibroblasts (wild-type – WT) (gift from Dr. Carlos Lopez-Otin). These are the only NGPS cells available

to the scientific community, as non-immortalized primary cells could not be maintained in culture (personal communication from Dr. Carlos Lopez-Otin). We observed severe NE abnormalities by electron microscopy, including deep folds and NE blebbing but no apparent loss of heterochromatin at the nuclear periphery (Fig. 1A). The immortalized NGPS cells proliferated at a rate comparable to WT cells. As previously reported (*4, 23*), we confirmed the accumulation of the NE protein emerin into the cytoplasm of both NGPS1 and 2 (Fig. 1B), and the absence of lamin B1 downregulation (Fig. 1B) and of DNA double strand breaks accumulation (53BP1 foci Fig. 1C, D), both of which being common hallmarks of HGPS cells. In addition, and unlike HGPS cells, NGPS fibroblasts did not display loss of nuclear Ran – used as a reporter for nucleocytoplasmic transport (Fig. 1C, E) or of the heterochromatin markers HP1γ (Fig. 1F-I), H3K9me3 (Fig. 1J and Supplementary Fig. 1A-C) or H3K79me2 (Fig. 1K). We did however observe an increase in the expression of the cyclin-dependent kinase inhibitor p21 – involved in cell cycle progression, apoptosis and DNA damage response – in both NGPS cell lines but to different extents (Fig. 1L and Supplementary Fig. 1D, E).

A combination of four specific NGPS phenotypes amenable to high-throughput screening

Phenotypes associated with NE dysfunction in progeria cells can only be assessed by microscopy, precluding a whole genome pooled CRISPR screening approach. We therefore designed a multiparametric, microscopy based CRISPR screen, aimed at interrogating the whole genome to identify genes that when deleted, could rescue multiple NGPS cellular phenotypes. This approach is based on the principle of synthetic rescue, relying on a genetic interaction whereby a protein not involved in the aetiology of the disease is targeted, thereby rebalancing the pathophysiological state towards a “healthy” one. Our previous work, based on small scale screening, has established the proof-of-concept of this approach in HGPS, where we identified N-acetyltransferase 10 (NAT10) as a target to reverse HGPS aging phenotypes

(*24-26*). The design of the screen is depicted in Fig. 2A and involves multiple steps. The first major step relied on the identification of a combination of phenotypes, specific to the BAF A12T mutation, significantly different in NGPS cells compared to WT cells, and amenable to high throughput screening. To this aim, we took advantage of our recently established NGPS2 isogenic cell lines, in which we reversed the homozygous BAF A12T mutation using CRISPR/Cas9 (NGPS2 corrected) (*14*). For this reason, we carried out further validation using the NGPS2 cell line. The screen set-up also required the design of specific pipelines to reliably identify and quantify these phenotypes. The first of these phenotypes is the delocalization of emerin from the nucleus into the cytoplasm (Fig. 2B-C and Supplementary Fig. 2A), as characterized by previous studies (*4, 23*). The second phenotype is the increased nuclear deformation, commonly observed in progeria cells (*17, 27*) and in cells from normal aged individuals. This was measured using a perimeter to area ratio (P2A) (Fig. 2D and Supplementary Fig. 2B). Additionally, we identified an increased number of NE ruptures during interphase in NGPS cells (Fig. 2E and Supplementary Fig. 2C), further characterized in our recently published study (*14*). In that study, we showed that the BAF A12T mutation in NGPS cells affects the binding affinity between BAF and Lamin A/C, preventing the recruitment of Lamin A/C to the sites of NE ruptures, leading to frequent NE re-rupturing in interphase cells. Based on these findings, here we identified NE ruptures on fixed cells by the presence of nuclear blebs (observed using LAP2 staining), the first step in the NE rupturing process (*28-30*) (Fig. 2E, F, H). Finally, we observed an increased frequency of micronuclei formation in NGPS cells (Fig. 2G, I and Supplementary Fig. 2D), a known marker of genomic instability. The combination of these four phenotypes was subsequently chosen for the whole genome screen.

Next, we engineered stable Cas9 expression in WT and NGPS fibroblasts for use in the CRISPR screening. After testing the efficiency of protein transduction using various promoters

(Supplementary Fig. 3A, B) we infected WT and NGPS cells with hCMV-Cas9. Despite a good Cas9 expression level in all three cell lines (Supplementary Fig. 3C), the knock-out efficiency in individual cells was too heterogenous for screening purposes (Supplementary Fig. 3D). Therefore, we established individual WT and NGPS Cas9 expressing clones grown from single cells and selected the best clones based on Cas9 efficiency assessed by resistance to 6-Thioguanine after *HPRT* knock-out (*31*) (Supplementary Fig. 3E-G). We also assessed Cas9 expression level by western blotting (Supplementary Fig. 3E) and picked clones combining a high cutting efficiency, and no increase in the level of the DNA double strand break marker γH2AX (Supplementary Fig. 3E, F). Finally, to avoid obtaining results that could result from a clonal effect, we pooled 3 of the selected clones to generate the WT-Cas9, NGPS1-Cas9 or NGPS2-Cas9 cell populations. The NGPS2-Cas9 was the one used for the screen and was generated by pooling clones D, F and I (Supplementary Fig. 3E-G). These Cas9 cells showed a good level of protein knock-down upon transient transfection with various crRNAs (Fig. 2J – acetyl-tubulin level serves as an additional readout for *HDAC6* knockout efficiency).

Finally, as the project started at a time when the first whole genome CRISPR arrayed libraries were being synthetized, we tested the efficiency of the two non-viral systems available at the time, one relying on a CRISPR/tracrRNA (cr/tracrRNA), the other one on a single guide RNA (sgRNA). After comparing the knock-down efficiency of several genes by western blotting (Supplementary Fig. 3H) and by immunofluorescence (Fig. 2K and Supplementary Fig. 3I-L), we set up a mini screen relying on cellular proliferation arrest upon knock-down of five different mitotic genes, compared to 5 non-mitotic genes (Fig. 2L). In both cases, we observed a strong proliferation arrest 3 days after transfection of either the sgRNA (Fig. 2L left panel) or the cr/tracrRNA (Fig. 2L right panel) against the mitotic genes (blue/purple genes), without transfection-associated toxicity (grey/red/yellow genes). Based on cost efficiency, we therefore selected the cr/tracrRNA system for the whole genome screen.

The multiparametric NGPS screen identifies 43 hits that reverse NGPS phenotypes

We then carried out the primary genome wide screen using the pool of 3 NGPS2-Cas9 expressing clones (NGPS2-Cas9). An overview of the screening approach is depicted in Fig. 3A, and the plate layouts are shown in Supplementary Fig. 4A-B. The four screening phenotypes - nuclear shape, micronuclei, NE ruptures (blebs) frequency and emerin nuclear intensity - were reduced to two dimensions for each single knock-out and mapped as a Uniform Manifold Approximation and Projection (UMAP). The cluster analysis (Fig. 3B) was used to visualise NGPS2 cells (grey dots) alongside the same parameters measured in control cells (blue dots). The two populations were clearly separated, reflecting the phenotypic difference between the control and the NGPS2 cells. The red dots highlight 112 genes that upon being depleted were identified as "normalising" the combination of NGPS phenotypes. To these, we added 18 genes not yet on the list that appeared in the top 15 of three individual phenotypes (see details in the Methods section). The top 20 genes improving or worsening each individual phenotype in NGPS cells (nuclear shape, nuclear Emerin, micronuclei and nuclear bleb frequency) is presented in Fig. 3C-F.

We then carried these 130 genes into a validation screen, in which 3 out of the 4 individual crRNAs used in the primary screen were deconvoluted into individual wells (Fig. 3A). We carried out the validation screen in triplicate and confirmed 43 hits with high confidence (at least 2 out of 3 crRNA and confirmed in the 3 replicates). A gene ontology analysis revealed specific enrichment in biological processes including translation, protein and RNA transport as well as osteoclast development – of high relevance to the patient phenotypes (Fig. 4A, B)**.** In accordance with the concept of synthetic rescue, only 3 hits were proteins associated with the NE: NUP160, SEC13 and AHCTF1 (ELYS). These genes were able to improve multiple

nuclear envelope phenotypes at once, as observed in representative immunofluorescence images from the validation screen (Fig. 4C).

To evaluate the potential relevance of our identified candidate genes to normal variation in related health and disease traits, we interrogated phenotypic and genetic data from available large-scale population studies. These analyses aim to assess the impact of naturally occurring alleles, influencing the function of our candidate genes, on related phenotypes. Since NGPS patients display severe skeletal abnormalities and lipoatrophy, we focused on publicly available Genome Wide Association Studies (GWAS) of body mass index (BMI), waist-hip ratio (WHR) adjusted for BMI, circulating triglyceride levels and estimated bone mineral density (eBMD) in sample sizes up to 1,253,275 individuals (Fig. 4D). We found that 30 of our 43 identified genes were within 500kb of a genome-wide significant signal for at least one of these four traits. Specifically, 13 genes were proximal to BMI signals, 11 to WHR, 19 to eBMD and 13 to triglyceride signals (Supplementary Data 8 & Fig. 4D). To more directly link these proximal associated genetic variants to the function of our candidate genes, we undertook a number of variants to gene mapping approaches (see methods), including assessment of protein-coding variants and integrating activity-by-contact enhancer maps and expression quantitative trait loci (eQTL) data. These analyses highlighted a number of genes with strong support for a direct involvement in these human phenotypes (Fig. 4D). For example, genetic variants residing within enhancers for *RPL13* and influencing its transcript expression in blood, were associated with eBMD, triglycerides and BMI. Collectively these findings demonstrate that our cellular

screens are able to identify genes that influence NPGS-like phenotypes in the normal population.

Increased protein synthesis rate associated with BAF A12T is reduced upon depletion of the hits

The screen revealed a strong enrichment for genes involved in protein synthesis, whose modulation has previously been associated with longevity in various model organisms. To gain further insights into protein synthesis regulation in NGPS, we first carried out RNA-Seq analysis in wild-type cells compared to NGPS1 and NGPS2. The analysis revealed 213 genes as being differentially expressed in the patient cell lines compared to control. Gene ontology analysis identified a strong enrichment for RNA processing and translation regulation (Fig. 5A-B). To assess how this could impact translation rate, we measured nascent protein synthesis using incorporation of the clickable methionine analogue L-homopropargylglycine (HPG). Upon fluorescent labeling of HPG through a "click" reaction, we observed a significant increase in protein synthesis in NGPS cells compared to both WT cells and NGPS corrected cells (Fig. 5C, Supplementary Fig. 5A) as well as in wild-type fibroblasts overexpressing BAF A12T compared to BAF WT (Fig. 5D, Supplementary Fig. 5B). This suggests that the BAF A12T mutation can drive increased protein synthesis, similarly to what has been reported previously in HGPS cells (*33*). However, even though we observed a modest but significant increase in the nucleolar area of NGPS2 cells compared to NGPS2 corrected cells (Fig. 5E-F), as well as in fibroblasts expressing BAF A12T compared to BAF WT (Fig. 5G), no significant difference was observed between the WT cells and the NGPS cells (Supplementary Fig. 5C, D). Interestingly, alongside this phenotype, we identified through a dual luciferase mistranslation assay (*34*) that both NGPS1 and NGPS2 cells displayed an increased rate of

errors during protein synthesis, as observed by an increased readthrough (Fig. 5H, Supplementary Fig. 5E).

We next asked how depletion of the hits identified in the screen might impact nascent protein synthesis in NGPS cells. To address this question, we used siRNA to deplete 41 of the hit proteins, followed by HPG incorporation and quantification of HGP fluorescent intensity by high-throughput microscopy (Fig. 6A, Supplementary Fig. 5F). This confirmed a higher rate of protein synthesis in NGPS2 cells (Fig. 6A red dotted line) compared to NGPS2 corrected cells ("NGPS WT"). As expected, depletion of the hits directly involved in protein synthesis (*RPL12, RPL37A, RPL13, RPS3A, EIF3B*) almost completely abolished HPG incorporation, and served as a good positive control for the assay. Interestingly however, we observed that depletion of many of the other hits, not known to play a direct role in protein synthesis, also led to a reduction of HPG incorporation to various extents in NGPS2 cells, with 21 genes out of the 43 hits (49%) reaching significance (Fig. 6A, blue data points). To assess the potential link between the reduction of protein synthesis we observed in NGPS2 upon depletion of the hits and the phenotypic improvements identified in our whole genome screen, we treated NGPS1 and 2 cells with the protein synthesis inhibitors cycloheximide (CHX) and silvestrol. Both inhibitors led to the enrichment of emerin into the nucleus of NGPS1 and NGPS2 cell lines (Fig. 6B-C).

Depletion of RPS3A, PAFAH1B1, VPS16 and SMU1 suppress the lethality of an NGPS *C. elegans* model

To establish the potential of our screen hits in translating into improvement of NGPS phenotypes *in vivo*, we used an NGPS *C. elegans* model (hermaphrodites) carrying a *baf-1(G12T)* mutation. We have recently reported the phenotype of these NGPS worms (*35*). Interestingly, the NGPS worms have a shorter lifespan and recapitulate the phenotypes we

observed in the patient cells, including loss of emerin from the NE, accumulation of misshapen nuclei, and deregulation of ribosomal genes (*35*). This model therefore strongly supports the relevance of the phenotypes and the mechanisms we identified in the patient cells in this study. In accordance with the nucleolar size changes we observed in NGPS cells (Fig. 5E-F), control of nucleolar size appeared to be impaired in *C. elegans* too. Indeed, in hypodermal nuclei of live NGPS (G12T) *C. elegans* expressing a GFP tagged nucleolar marker, we observed an increased nucleolar area compared to wild-type (WT) worms (Fig. 7A-B). The *baf-1(G12T)* mutant worms are fully viable, but <10% complete development when combined with an endogenously tagged *gfp::lmn-1*/lamin allele (Fig. 7C, Supplementary Fig. 6A). We took advantage of this sensitized background to test for rescue of developmental arrest upon RNAi-mediated knockdown of 32 genes from our screen (Fig. 7C and Supplementary Fig. 6B), for which there was a *C. elegans* homologue. Interestingly in regards to the protein synthesis data we obtained in human cells, depletion of RPS-1 (the *C. elegans* homologue of human RPS3A), a ribosomal protein of the 40S subunit, suppressed the lethality of the *gfp::lmn-1; baf-1(G12T)* animals (Fig. 7B). Three additional genes: *lis-1* (PAFAH1B1) – involved in various dynein and microtubule processes as well as in osteoclast formation (*36*), *vps-16* (VPS16) – a protein involved in protein trafficking to lysosomal compartments (*37*), and *smu-1* (SMU1) – involved in mRNA splicing (*38, 39*), led to a similar rescue of worm lethality (Fig. 7C). Depletion of the other genes did not rescue the lethality (Supplementary Fig. 6B), potentially due to some of them – including protein synthesis genes – being essential *in vivo*.

DISCUSSION

Our data demonstrates the feasibility and the power of a microscopy based, CRISPR/Cas9 genome-wide screen for suppressing and bypassing progeric phenotypes in patient-derived fibroblasts. While a targeted (320 genes) multiparametric siRNA screen has been carried out

previously in a cellular model of HGPS (*40*), our screening approach has interrogated the entire human protein coding genome (19,200 genes) and used NGPS patient cells. The only patient-derived cells currently available are immortalized fibroblasts, due to the inability of the primary cells to grow in culture (personal communication from Carlos Lopez-Otin). This prevents the possibility to perform functional assays such as replicative lifespan in culture or migration assays which is one caveat of the current study. On the other hand, immortalized cells are much more amenable to large scale screening assays such as the one we performed here, especially when considering the fact that we had to establish Cas9 expressing clones grown from single cells – which would have been very challenging with primary patient fibroblasts. By using both WT fibroblasts from an unaffected individual, as well as NGPS fibroblasts in which we reversed the BAF A12T homozygous mutation using CRISPR/Cas9 (*14*), we were able to identify a reliable combination of four cellular phenotypes that were both specific to the BAF A12T mutation, and quantifiable by high throughput microscopy. This approach allowed us to reduce the number of hits to ~0.2% of the whole genome library, and to identify genes showing the best "rescue" across several phenotypes. In accordance with the principle of synthetic rescue, only 3 of the hits were NE proteins, and more specifically nuclear pore complex proteins: NUP160, SEC13 and AHCTF1 (ELYS). Both SEC13 and ELYS have been previously shown to regulate nuclear size and nuclear import (*41*), a function shared by RAN, another hit from our screen. This suggests that modulating nuclear import might have positive effects on NE organization and function in NGPS cells.

In view of the strong skeletal abnormalities of NGPS patients, it is also worth highlighting that our screen identified two genes involved in osteoclast development: *LRRK1* (Leucine-rich repeat serine/threonine-protein kinase 1) and *PAFAH1B1/LIS1* (Platelet-activating factor acetylhydrolase IB subunit alpha), whose depletion improve NGPS cellular phenotypes (Fig. 3 and 5) and in the case of LIS1 also increases viability of NGPS worms (Fig. 7C). LRRK1 has

been involved in the regulation of osteoclast activity and bone resorption (*42-44*). Accordingly, LRRK1 dysfunction in mice or human is associated with severe osteopetrosis (*4*5). Similarly, PAFAH1B1 regulates osteoclast formation and bone homeostasis through interacting with the protein Plekhm1, involved in osteoclast secretion. PAFAH1B1 depletion has been shown to strongly reduce osteoclast formation (*36*). Therefore, we can hypothesize that the severe osteoporosis and osteolysis observed in NGPS cells might be associated with an increased level or activity of LRRK1 and/or PAFAH1B1. This might contribute to the aberrant NGPS cellular phenotypes that become normalized upon depletion of these genes. As a follow up experiment, it would be interesting to study the effect of the BAF A12T mutation in bone-derived cell lines, and establish the benefit of LRRK1 and PAFAH1B1 depletion to the response of these cells to mechanical stress for example. Once a mouse model for NGPS becomes available, it would be of course also very relevant to test how modulating these genes might improve the phenotypes of the mice in vivo.

Here, we decided to exploit *C. elegans* to perform functional assays, due to the absence of primary NGPS cells (as described above), and because it is a highly appreciated model to study mechanisms of aging. Numerous studies have concluded that interventions that either extend or shorten lifespan in worms have similar effects in other animals, including mammals *(46-48)*. Secondly, the strong conservation of *BAF* across the animal kingdom both in terms of primary amino acid sequence and predicted secondary structure argues in favour of functional conservation. For instance, it has been shown that phosphorylation of BAF by the kinase VRK1 regulates BAF dynamics similarly in worms, flies, and human cells. In addition and supporting this idea, our recent work (*35*) shows that the NGPS *C. elegans* model recapitulates phenotypes of the NGPS patient fibroblasts. These include deterioration of nuclear morphology with age, decreased emerin incorporation at the NE, enlarged nucleoli and deregulation of ribosomal

genes. These phenotypes are associated with a decreased lifespan and altered resistance to stress.

One of the top functional enrichments in the screen was protein synthesis, with 7 out of the 43 hits being associated with this process. Loss of protein homeostasis is one of the hallmarks of aging (*19*) and inhibition of translation has been associated with enhanced longevity in several animal models (*49-51*). Identifying that inhibition of this pathway was beneficial to NGPS cells and NGPS worms, therefore reinforce the current hypothesis that loss of cellular homeostasis observed in both premature and physiological aging might occur through similar mechanisms. More specifically, we observed that the NGPS associated BAF A12T mutation was associated with a higher rate of nascent protein synthesis, together with differential expression of genes involved in translation regulation (Fig.5A-D). Our recently published paper (*35*) also shows that the A12T mutation directly affects the DNA binding profile of BAF, leading to differential expression of genes involved in ribosomal structure and translation. Interestingly, almost all ribosomal genes that were found to be differentially expressed in the NGPS worms, associated less frequently with BAF-1(G12T) than with BAF-1 wild-type. This suggests that the BAF A12T mutation may indirectly impact translation by modulating its DNA binding profile, therefore modifying the expression of translation-associated genes. Translation deregulation – potentially occurring through different mechanisms - could therefore be a common process contributing to premature aging, as increased protein synthesis was also observed in primary HGPS cells and was similarly acoompanied by increased nucleolar size (*33*). In the case of NGPS, we saw that this was associated with a higher rate of errors, as seen by an increased stop codon readthrough. It therefore appears that fibroblasts derived from both HGPS and NGPS patients go through a phase of enhanced protein synthesis while they are still in a replicative state (low passage number in the case of primary HGPS cells or immortalization in the case of NGPS). As translation is one of the most energy consuming process in the cell, this

could accelerate cell exhaustion, contributing to premature entry of the cells into senescence. Once the cells enter into senescence, they then display reduced global protein synthesis. As the NGPS cells are immortalized, we cannot assess the effect of protein synthesis reduction on the replicative lifespan of the cells in culture, and therefore we cannot connect the phenotypic rescue to cellular senescence.

There is currently no mouse model for NGPS but a recent study reported the effect of error-prone protein synthesis in mice (*52*). Through engineering a specific ribosomal mutation, the authors induced genome-wide translational errors in mice. This resulted in reduced lifespan and premature aging features resembling the phenotypes observed in NGPS patients including chest and spine deformation as well as loss of fat. This suggests that deregulation of protein synthesis and accumulation of errors might directly contribute to the premature aging phenotypes of NGPS patients. Therefore, identifying non-toxic pharmacological interventions to slow down protein synthesis, thereby potentially limiting error-prone translation might yield phenotypic improvement at the level of the individuals. According to our data, this could be achieved through targeting proteins directly involved in protein synthesis (such as RPL proteins) as well as proteins involved in various other cellular functions (Fig. 5G). Indeed, in the cellular context of NGPS, we observed a reduction of nascent protein synthesis upon depletion of genes that don't have any known protein synthesis function. The mechanisms behind this and the link between protein translation and NE integrity remain unknown and will be the basis of future studies, but it does suggest a common mechanism by which depletion of the hits from the screen improve NGPS phenotypes.

Altogether, our screen has shed light on pathways involved in cellular dysfunction caused by the BAF A12T mutation in NGPS patient cells. This work has also identified potential therapeutic targets for this incurable premature aging syndrome, supported by the data we

obtained *in vivo*, showing rescue of lethality in NGPS worms upon knocking down some of the hits from the screen.

METHODS

Ethics

Our research complies with all relevant ethical regulations. The NGPS-derived patient cells were obtained from Prof. Lopez-Otin with informed consent from the patients and ethical oversight.

Cell culture

Wild type (WT, derived from an age-matched healthy individual (AG10803, Coriell repositories), NGPS5796 (NGPS 1) and NGPS5787 (NGPS 2) - both males - immortalized fibroblasts were a kind gift of Prof. Carlos López-Otín (University of Oviedo, Spain). All three cell lines were immortalized with SV40LT and TERT. Cells were grown at 37°C in a 5% CO_2 incubator in Dulbecco's modified Eagle's medium containing 4.5 g/L glucose (Sigma) supplemented with 2 mM L-glutamine (Sigma), 10% foetal bovine serum, 100 units/mL penicillin and 0.1 g/L streptomycin (complete medium). WT cells expressing Flag-BAF or Flag-A12T BAF were described before (14) and maintained in complete medium containing 100 μg/mL hygromycin B (Toku-E, #H007, made up to 100 mg/mL in PBS). Cells were passaged twice a week and used within 12 passages. Cells were free of mycoplasma as assessed using strips (InvivoGen #rep-mys-20). For the phenotypic comparison with HGPS (Figs. 1 and S1), WT cells were GM05565 fibroblasts and HGPS cells were AG11513 cells, both obtained from Coriell Institute for Medical Research (Camden, New Jersey, U.S.A.).

Antibodies and Reagents

Supplementary Table 1 lists antibodies and reagents used in Western blotting (WB) and immunofluorescence (IF) applications.

Immunofluorescence

Cells were seeded on thickness 1 ½ round coverslips (Thermo Fisher Scientific) in 12-well plates for full-field imaging, thickness 1 ½ square (18 mm x 18 mm) coverslips (Zeiss) in 6-well plates for super-resolution imaging or in a 96-well view-plate (PerkinElmer #6005182) for high-content imaging and grown to a confluency level consistent across the cell lines to be compared. All subsequent steps were carried out at room temperature. Cells were fixed with 4% paraformaldehyde in PBS (Boster, AR1068) for 20 minutes, followed by permeabilization in 0.2% Triton X-100 in PBS for 12 minutes. Unspecific antibody binding was blocked by incubating in 5% BSA (Sigma #A7906), 0.1% Tween-20 in PBS (IF blocking buffer) for 30 minutes. Primary antibodies were diluted in IF blocking buffer (see Supplementary Table 1) and incubated for 1-2 hours. After 3 washes with PBS cells were incubated with secondary antibodies and DAPI diluted (see Supplementary Table 1) in IF blocking buffer. After 3 washes with PBS coverslips were mounted using Prolong Gold (P10144) and left to set at room temperature overnight; cells stained in 96-well plates were overlaid with 100 μL/well fresh PBS and stored at 4°C until imaging. Wide-field immunofluorescence imaging was on an upright Axioimager Z2 (Zeiss) using a Hamamatsu Flash 4 sCMOS camera and Zeiss plan-apox lens, 63x 1.4 N.A. oil immersion objective and ZenBlue 2012 image acquisition software. Super-resolution imaging was on an Elyra PS1 structured illumination microscope (Zeiss) using a ZenBlack SR edition image acquisition software (Zeiss), PCO edge 4.2 sCMOS camera and 63x 1.4 N.A. oil immersion objective. High-content imaging was on a CellInsight CX7 microscope (Thermo Fisher Scientific) using a 20x 0.35 N.A. objective. HCS Studio software 2021 (Thermo Fisher Scientific) was used for quantitative image analysis. For quantitation of H3K9me3 or HP1γ nuclear intensities the DAPI images were used to define the nuclear contour, and a fixed intensity threshold was set to define the stained heterochromatin domains.

Western blotting

Confluent monolayers of cells in 6-well plates were washed with PBS and scraped in 70 μL/well SDS lysis buffer (4% SDS, 20% glycerol, and 120 mM Tris-HCl (pH 6.8)). Lysates were incubated for 5 min at 95°C. The DNA was sheared by syringing 10 times through a 25-gauge needle. Absorbance at 280 nm was measured (NanoDrop, Thermo Fisher Scientific) to determine protein concentration. Samples were prepared in NuPAGE sample buffer (Thermo Fisher Scientific #NP0007) and DTT (100 mM) and heated at 95°C for 10 min. Proteins were loaded on NuPAGE 4-12% Bis-Tris gels (Thermo Fisher Scientific), separated in NuPAGE MES SDS running buffer (Thermo Fisher Scientific #NP0002) and transferred to 0.2 μm pore size nitrocellulose membranes (Amersham, #10600004) for immunoblotting. Blotted proteins were reversibly stained with Ponceau S solution (Thermo Fisher Scientific, # A40000279) to allow cutting strips for individual antibody incubations. Membrane strips were first blocked for 30 min in 5% milk in TBST buffer (20 mM Tris, 150 mM NaCl, 0.1% Tween-20) before incubation with primary antibodies diluted in TBST buffer (see Supplementary Table 1) for 1h at room temperature. After 3 washes with TBST buffer membrane strips were incubated for 1 h with IRDye-conjugated secondary antibodies (LI-COR, see Supplementary Table 1). After 3 more washes with TBST buffer membrane fluorescence was scanned on an Odyssey CLx imaging system (LI-COR).

Transmission electron microscopy

Cell monolayers were fixed by the addition 2.5% glutaraldehyde / 2% paraformaldehyde in 0.1M Na cacodylate buffer, pH 7.2 at 37°C. The monolayer was then scraped from the tissue culture plastic, pelleted in a benchtop microfuge and allowed to cool to room temperature.

The cell pellet was washed with 0.1M Na cacodylate buffer, pH 7.2; post-fixed in 1% osmium tetroxide in 0.1M Na cacodylate buffer, pH 7.2, for 1 hour, and washed with 0.05M Na maleate

buffer, pH 5.2. Next, the cells were stained en bloc with 0.5% uranyl acetate in 0.05M Na maleate buffer, pH 5.2, for 1h at 4°C; washed with 0.05M Na maleate buffer, pH 5.2; dehydrated in a graded series of ethanol and exchanged into 1,2-epoxy propane. The cell pellet was then infiltrated with 50:50 epoxy propane: Agar 100 resin overnight before exchange into Agar 100 resin. Finally the cell pellets were embedded in Agar 100 resin in BEEM capsules (Agar Scientific, Stansted, UK) overnight at 60°C. Ultrathin sections (60nm) were cut using a diamond knife mounted on a Leica Ultracut UC7 ultramicrotome (Leica, Milton Keynes, UK), collected on formvar-coated copper EM grids and stained with uranyl acetate and Reynolds lead citrate. The sections were observed in an FEI Tecnai G2 Spirit BioTWIN transmission electron microscope (Eindhoven, The Netherlands) at an operating voltage of 80 kV. Images were captured using a Gatan US1000 CCD camera.

Generation of Cas9-expressing cells

Stable Cas9 expression was engineered in the WT and in both NGPS cell lines as follows. We first assessed protein expression efficiency from seven constitutive promoters (hCMV, mCMV, hEF1a, mEF1a, CAG, PGK and UBC) using a SMARTchoice promoter selection plate (Horizon Discovery, #SP-001000-01). The hCMV promoter showed the highest expression and was chosen to drive Cas9 expression. WT and NGPS cells were transduced with purified lentiviral particles, containing a vector encoding the S. pyogenes Cas9 nuclease under the control of a hCMV promotor according to the manufacturer's protocol (Horizon Discovery, #VCAS10124). Cells stably expressing Cas9 were selected using 5 µg/mL blasticidin (Merck/Sigma Aldrich), and several clones were isolated from the polyclonal population by single cell sorting. Individual clones were assessed for Cas9 expression, cellular morphology, effect on cell health markers such as DNA damage (gH2AX level) and proliferation, as well as Cas9 cutting efficiency. The latter was assessed based on resistance to 6-thioguanine upon

HPRT knock out as described before (31) as well as by knock down efficiency using immunofluorescent staining or Western blotting (see CRISPR mini-libraries and Supplementary Table 2). Based on these, to avoid any clonal effect that might arise from a single clone, three Cas9-expressing clones were selected for each cell line and pooled for further CRISPR experiments (WT-Cas9 or NGPS-Cas9) including the mini-libraries and genome-wide screens.

CRISPR mini-libraries

Two CRISPR mini libraries were obtained; one contained pools of 3 sgRNAs targeting 10 genes (Synthego, Redwood City, CA, USA) (Supplementary Table 3), the other contained pools of 4 crRNAs targeting 20 genes (Horizon Discovery, Waterbeach, UK) (Supplementary Data 1). For immunofluorescence or cell proliferation assays, WT-Cas9 or NGPS-Cas9 cells were reverse transfected with the CRISPR reagents in a 96-well view-plate (Perkin Elmer #6005182). Per well 20 μL transfection mix was first prepared in a V-bottom 96-well plate (Greiner #651161) as follows. For crRNA:tracrRNA transfection, 2.5 μL 1 μM crRNA and 2.5 μL 1 μM trRNA were added to 5 μL Optimem; for sgRNA transfection 2.5 μL 1 μM sgRNA was added to 7.5 μL Optimem. To each well containing 10 μL diluted crRNA:tracrRNA or sgRNA was then added 10 μL of a Dharmafect-1 dilution (0.05 μL Dharmafect-1 in 9.95 μL Optimem). The solutions were mixed by pipetting up-and-down and incubated for 20 minutes at room temperature before arraying in a 96-well view-plate (Perkin Elmer #6005182). Meanwhile, cell suspensions were counted using a Countess cell counter (Thermo Fisher Scientific) and dilutions prepared such that to each well were added 3300 cells for WT-Cas9 and NGPS2-Cas9 or 5000 cells for NGPS1 cells in a 80 μL volume in antibiotic-free growth medium. Plates were shaken by hand and placed in a 37°C incubator for 65-72 hrs. For cell survival analysis plates were put in an Incucyte live-cell imaging incubator 24 hrs post-

transfection (see Cell proliferation). For Western blotting analysis of sgRNA-transfected cells, reverse transfections were carried out in 12-well format. Per well 3 μL 10 μM sgRNA was diluted in 50 μL Optimem, incubated for 5 minutes before adding diluted Dharmafect-1 (0.6 μL Dharmafect-1 in 50 μL Optimem). Transfection mixes were overlaid with 900 μL antibiotic-free growth medium containing 120,000 NGPS1-Cas9 cells. Plates were shaken and put at 37°C for 72 hrs before cell lysis.

Cell proliferation (Incucyte)

WT or NGPS cells were seeded onto 24-well plates (Falcon, # 353047), placed in a live-cell imaging incubator (Incucyte S3, Essen, Germany) and imaged with a 10x phase objective every 4 hours for 96 hours. Incucyte S3 analysis software was used to measure and quantify cell density over time. For assaying the mitotic gene knock-outs in the CRISPR mini-libraries WT-Cas9 or NGPS-Cas9 cells were reverse transfected in 96-well view-plates (Perkin Elmer #6005182) and placed in the Incucyte imaging incubator 24 hours post-transfection.

CRISPR library

A genome-wide CRISPR library was obtained from Horizon Discovery (GP-004650-E2-01, GP-004675-O2-01 and GP-006500-O2-01). The library was arrayed in 61 384-well plates and contained 4 unique crRNAs per gene per well, targeting a total of 19,127 human genes (Supplementary Data 2). Some crRNA pools were present in duplicate or triplicate, providing internal controls for the screen. The 0.1 nmole crRNA pools were resuspended in 20 μL 10 mM Tris buffer (Horizon Discovery #B-006000-100) to yield a 5 μM master plate. This master plate was further aliquoted into mother plates. To one mother plate containing 2.4 μL/well crRNA was added 21.6 μL 0.56 μM tracrRNA (Horizon); the resulting 24 μL of 0.5 μM crRNA:tracrRNA solution was then divided over transfection-ready daughter plates, each

containing 6 µL of 0.5 µM crRNA:tracrRNA per well. All liquid-handling steps were carried out using a CyBio Felix liquid handling robot (Analytik Jena, Jena, Germany). Plates were spun for 2 minutes at 300 x g, sealed using clear polypropylene seals (Starlabs E2796-0793) and stored at -30°C.

Genome-wide CRISPR screen

The genome-wide CRISPR screen was carried out with the NGPS2-Cas9 pool of 3 clones. Library plates containing transfection-ready crRNA:tracrRNA complexes were thawed and spun at 300 x g for 3 minutes. Emerin and non-targeting crRNA:tracrRNA complexes were added to columns 23 and 24 (see plate layout, Fig. S3A) as positive controls for the transfection efficiency and negative controls respectively. For reverse transfection, Dharmafect-1 (Horizon Discovery) was diluted in Optimem (Thermo Fisher) (120 µL in 23.88 mL Optimem) and incubated for 5 minutes at room temperature before distributing in a 384-well plate. A liquid handling robot (CyBio Felix, Analytik Jena, Germany) was used to add the Dharmafect 1 solution to the crRNA:tracrRNA complexes and to mix the 2 solutions. After 20 minutes of incubation at room temperature, the transfection mixes were distributed in 384-well imaging plates (Greiner #781182) and overlaid with 1200 NGPS2-Cas9 cells/well in 30 µL of complete DMEM medium. WT cells and NGPS2 WT cells (from the 2 clones in which the BAF A12T mutation was reversed using CRISPR Cas9 (14) – see Fig. S3A) were added in columns 1 and 2 of each plate (that do not contain transfection complexes). Plates were then kept in a 37°C incubator with 5% CO_2 for 72 hours. All subsequent steps were carried out at room temperature. Cells were fixed using a Wellmate robot (Thermo Fisher) by adding 30 µL/well of 4% PFA for 30 minutes. Fixative was removed through plate inversion, cells were washed once with 40 µL/well PBS and permeabilized with 40 µL/well of 0.2% Triton X-100 in PBS for 12 minutes. Unspecific antibody binding was blocked by incubation for 30 minutes with IF

552 blocking buffer (see Immunofluorescence). Next, cells were incubated for 1 hour with a
553 mixture of primary antibodies (20 µL/well) diluted 1:1000 in IF blocking buffer: rabbit anti-
554 emerin, mouse IgG_{2b} anti-lamin A/C and mouse IgG_1 anti-LAP2 (details in Supplementary
555 Table 1). Following a wash with PBS (40 µL/well), cells were incubated for 1 hour with a
556 mixture of secondary antibodies (Alexa Fluor 488 anti-mouse IgG_{2b}, Alexa Fluor 568 anti-
557 mouse IgG_1 and Alexa Fluor 647 anti-rabbit – details in Supplementary Table 1), as well as
558 DAPI (Supplementary Table 1), in IF blocking buffer (20 µL/well). After a final wash with 40
559 µL/well PBS the cells were overlaid with 40 µL/well fresh PBS, plates were sealed with a black
560 seal (Perkin Elmer) and loaded onto a OrbitorRS plate handling robot (Thermo Fisher) for
561 loading into and imaging using a CellInsight CX7 high-content microscope (Thermo Fisher).
562 4-channel images were acquired with fixed exposure times using a 20x 0.35 N.A. air objective
563 for 9 fields/well or until 500 nuclei ("objects") were detected in the DAPI acquisition channel.
564 The HCS studio colocalisation bio-application was used to calculate a nuclear shape parameter
565 for the DAPI-defined objects and the emerin intensity in both the nucleus, defined by the DAPI
566 mask, and in a cytoplasmic ring defined by expansion of the DAPI mask. For micronuclei
567 analysis, the LAP2 images were run through the HCS studio micronuclei bio-application. This
568 analysis module was further modified to detect nuclear blebs, again using the LAP2 images
569 (53). All primary screen results are collated in Supplementary Data 3.
570
571 Primary screen hit identification
572 Two multivariate analyses were carried out in R using custom scripts which are described here:
573 Raw genome-wide CRISPR screen data were read into R in a plate-by-plate basis. Control
574 wells were annotated before normalisation of emerin nuclear intensity, emerin ratio and nuclear
575 shape factor P2A values to the median of the corresponding value of the NGPS2 negative
576 control on each plate. Z scores were calculated (calculated by subtracting the mean of each

phenotype from each value and dividing by the standard deviation of each phenotype) and selected values plotted in S plots (supplementary figures x – y). For both multivariate analyses, data dimension reduction was achieved using UMAP (54) and clustering using k means, with optimal cluster number determined by manual determination of differential grouping of WT control samples to all other samples. A four-parameter (average nuclear emerin intensity, micronuclei frequency, nuclear shape factor P2A, and nuclear bleb frequency) analysis, including a scaling step prior to dimension reduction (subtraction of the values of each parameter by the mean of that parameter followed by division of the values of each parameter by the standard deviation of each parameter), yielded 51 hits. A three-parameter analysis, excluding emerin nuclear intensity as few gene knockouts rescued the phenotype, yielded 68 hits. Of the combined 119 hits we excluded genes whose knockout negatively affected cell survival or proliferation (nuclear count < 200), and we added genes not yet on the list that appeared in the top 15 of three individual phenotypes (nuclear shape factor, micronuclei or nuclear envelope bleb frequency), bringing the total number of hits taken forward for a deconvoluted validation screen to 130 (Supplementary Data 4). The scripts used in this study have been deposited on Zenodo and can be found here: https://doi.org/10.5281/zenodo.13927778.

Validation screen

For each of the 130 primary screen hits, 3 crRNA sequences were arrayed randomly in the central wells of two 384-well plates as a custom library (Horizon Discovery) (Supplementary Data 5). Control crRNA:tracrRNA complexes were added to the plates as detailed in Fig. S3B. Transfection, fixing, staining and imaging were all carried out as for the primary screen and repeated 3 times. Aggregate z-scores were calculated for the 3 sequences/genes for each phenotype (Supplementary Data 6). Genes whose z-score was below (for micronuclei

frequency, NE bleb frequency and nuclear shape parameter P2A) or above (for emerin nucleus:cytoplasm intensity ratio) the z-score for the NT control in the 3 repeat experiments were considered validated. The 43 validated genes are in the STRING diagram in Fig. S3C.

Nascent protein synthesis assay

Nascent protein synthesis was assayed using incorporation of the methionine analogue L-homopropargylglycine (HPG). Cells were grown in methionine-free medium (Thermo Fisher Gibco #21013-024) for 1 hour before incubation with 1 μM click-iT HPG (Thermo Fisher #C10428) in methionine-free medium for 1 hour at 37°C. All subsequent steps were carried out at room temperature. Cells were fixed with 4% paraformaldehyde in PBS for 20 minutes, followed by permeabilization with 0.2% Triton X-100 in PBS for 12 minutes. Next, a click reaction was allowed to proceed for 1 hour by incubation with 4 mM CuSO4, Alexa Fluor 488 azide (1:1000 dilution) and 10 mM sodium ascorbate in the dark. Click reagents were washed off and nuclei were stained with 0.2 μg/mL DAPI before imaging on the high-content microscope.

siRNA transfection

A custom siRNA mini-library containing On TargetPLUS siRNA smartpools (Horizon Discovery) targeting 41 of the 43 validated hits as well as some internal control genes (EMD, LMNA and TMPO (encoding LAP2)) arrayed in a 96-well plate was obtained (Supplementary Data 7, see Fig. S4F for the plate layout). The 0.1 nmole siRNA/well was diluted to 2 μM with 10 mM Tris buffer (Horizon Discovery #B-006000-100). Transfection mixes were prepared by adding diluted Lipofectamine RNAiMAX (Thermo Fisher Scientific) (1 μL in 33 μL Optimem) to diluted siRNA (5 μL 2 μM siRNA added to 28 μL Optimem) in a V-bottomed 96-well plate (Greiner #651161), mixing and incubating for 10 minutes at room temperature. 20 μL of the

transfection mix was then transferred to a 96-well viewplate well (Perkin Elmer #6005182) and overlaid with 80 μL cell suspension (NGPS2 cells, 3000 cells/well). siRNA transfection was allowed to proceed for 72 hrs before cells were assayed for nascent protein synthesis as detailed above.

Protein translation inhibition studies

WT or NGPS cells were seeded in 96-well imaging plates (PerkinElmer #6005182) and treated for 72 hours with 0.125 μg/mL cycloheximide (CHX, Sigma # C4859) or 2.5 nM silvestrol (Biovision #B2417-100) before staining and imaging as in the screens.

Protein mistranslation assay

WT or NGPS cells were seeded in 12-well plates. The next day cells were transfected with plasmid pRM hRluc-hFluc D357X, where Asp^{357} (GAC codon) was replaced by a UGA nonsense codon in the firefly luciferase (Fluc) transcript (34), using TransIT-2020 (Mirus #MIR5404) according to the manufacturer's protocol. 30 hours post-transfection cells were lysed in 200 μL/well passive lysis buffer (Promega #E1941) for 15 minutes at r.t. under gently rocking. Lysates from each 12-well were collected in 3 wells of a black 96-well plate (PerkinElmer #6005182) on ice. The activities of firefly and sea pansy (Renilla) luciferases were measured sequentially using reagents of the dual-luciferase reporter (DLR) system (Promega #E1910) with a ClarioStar plate reader (BMG Labtech Ltd., Aylesbury, U.K.). In brief, firefly luciferase activity was assayed through addition of 60 μL/well Luciferase Assay Reagent II. Next, firefly luciferase activity was quenched and Renilla activity measured by addition of 60 μL/well Renilla substrate in Stop&Glo buffer. As a positive control for translation errors cells were treated for 24 hours with 0.5 mg/mL G418 (Gibco # 10131035) prior to assaying.

RNA sequencing and analysis

Total RNA was extracted from wild type, NGPS1 and NGPS2 cells using the RNA extraction kit from Zymo Research. The RNA was analysed by Cambridge Genomics Services with Illumina TruSeq Stranded mRNA library prep kit. Input for libraries was 1µg for each sample. After the libraries were prepared, they were pooled in equal quantities and Quality Control was run including Bioanalyzer (average size 283bp) and qPCR (concentration 43nM). The RNAs were then sequenced using an Illumina NextSeq 500 2x75 cycles MID output kit. 2 pM of pooled libraries were loaded onto the sequencer and 1% Phix was added. FastQC (v0.11.4) was used to assess sequence quality and nucleotide content of paired-end fastq files and enabled trimming of low quality bases from the 3' end, using TrimGalore (v0.5.0). Trimmed reads were then aligned with STAR (v2.7.9) and HISAT2 (v2.1.0), for genome and transcript level analyses respectively, using Ensembl's Homo sapiens GRCh38 (release 109) reference files. Uniquely aligned genomic reads, with a mapping score of 10 or greater, were quantified using HTSeq (v0.6.1), while StringTie (v1.3.4) was used to assemble and estimate transcript expression levels of HISAT2 alignments. Read counts were then read into R statistical software (v 3.6.1) and used as input to the edgeR package (v3.26.5) for pairwise comparisons, to identify differentially expressed genes and transcripts between Wild type cells and NGPS1/NGPS2 cells. A '5 CPM (Counts Per Million) in at least half of the samples' filter was applied to the counts, which were then normalised before differential tests were performed. The CQN Bioconductor package (v1.30.0) was also used to correct for any Guanine-Cytosine or gene-length biases, prior to pairwise comparisons. Finally, p-values were adjusted for multiple testing via the False Discovery Rate (FDR; Benjamini-Hochberg) approach. Gene Ontology Analysis was performed on genes with a False Discovery Rate value less than 0.01.

677 Statistics

678 Statistical analysis was done using Graphpad Prism v9. The statistical test used is indicated in
679 the figure legends. Asterisks in the figures correspond to p-values as follows: * $0.01 \leq p < 0.05$,
680 ** $0.001 \leq p < 0.01$, *** $0.0001 \leq p < 0.001$, **** $p < 0.0001$. ns indicates a non-significant
681 statistical comparison.

682

683 Genome wide association studies (GWAS)

684 Target genes from the whole genome screen were integrated with common variant genome-
685 wide association studies (GWAS) and associated functional annotations, pertaining to coding
686 variants, expressions quantitative trait loci (eQTL) datasets and proximal enhancers.
687 For the common variant GWAS, we used data on body mass index (BMI, n= 806,834) and
688 waist-hip ratio (WHR) adjusted for BMI (n=694,649) from the GIANT study (55), the GLGC
689 triglycerides study (56) (n=1,253,275) and the GEFOS estimated bone mineral density (eBMD,
690 n=426,824) study (57) and only variants with a minor allele frequency >0.1%. For each of the
691 target genes and each phenotypic trait, genes were annotated based on proximity to genome-
692 wide significant signals ($p < 5x10^{-8}$), in 1Mb windows; 500kb up- or downstream of the genes
693 start or end site. As most GWAS signals are intronic or intergenic, we overlayed these
694 associations with other functional datasets to understand whether the associated variants can
695 be causally linked to changes in the identified genes' regulation or expression. First, we
696 calculated genomic windows of high linkage disequilibrium (LD; $R^2 > 0.8$) for each given
697 signal and mapped these to the locations of known enhancers for the target genes, using the
698 activity-by-contact (ABC) enhancer maps (32), to indicate whether the genomic variants
699 associating with the traits of interest directly changed the sequence of enhancers for the genes
700 in question. We then performed colocalisation analyses between the four GWAS and
701 expression quantitative trait loci (eQTL) data for genomic variants reaching at least a

suggestive level of significance in the GWAS ($p < 5x10^{-5}$), using the SMR and HEIDI tests (v1.02, (58)) and blood gene expression level data from the eQTLGen study (59). In doing so we essentially matched the pattern of association observed between the identified genomic variants and the GWAS outcome to the association towards the measured transcript level changes for the identified genes, to approximate the direct effect of the associated variants on the target gene expression. We considered gene expression of a gene to be influenced by the same genomic variation as that seen in the GWAS, if the FDR-corrected p-value for the SMR-test was $p<0.05$ and the p-value for the HEIDI test was >0.1%. Both of these sets of results allow us to draw methodological hypotheses about how genetic variants at the identified loci, can cause changes in the observed phenotypic traits, by directly affecting the genes regulation and expression patterns. Finally, we wanted to identify potential coding variants that might also associate with variation in the four phenotypes, indicating more direct protein-level consequences to the identified genes. To do this, we collapsed common coding variants within each of the identified genes and calculated gene-level associations towards each of the four traits, using a gene-level MAGMA analysis (v1.09) and SMR-HEIDI (v0.6886) (60). Genes exhibiting an FDR-corrected MAGMA p-value <0.05 were considered significant.

C. elegans maintenance

BN808 baf-1(bq19[G12T]) III was generated by backcrossing baf-1(G12T) mutants (six times with the N2 wild type strain. The baf-1(bq19[G12T]) allele contains two nucleotide substitutions at position 34-35 relative to the start codon (GG®AC) introduced by CRISPR/Cas9 genome engineering. BN1336 yc32[gfp::lmn-1] I; baf-1(bq19[G12T]) III was generated by crossing BN808 and UD484 (61) and balanced with hT2 [bli-4(e937) let-?(q782) qIs48] (I;III)). BN1389 knuSi221[fib-1p::fib-1::gfp + unc-119(+)] II; baf-1(bq19[G12T]) III was obtained by crossing BN808 and COP262 (62). These hermaphrodite strains were

maintained at 16°C on solid Nematode Growth Medium (NGM) plates seeded with *Escherichia coli* OP50 bacteria (63).

C. elegans nucleolar size measurement

Nucleolar area was quantified in the COP262 and BN1389 strains using the FIB-1::GFP reporter. Larvae were raised at 16°C and synchronized by picking L4 hermaphrodites and further incubated for 24 hours at 25ºC. Young adults were anaesthetized in a drop of 10 mM levamisole on top of soft agar pads as described (64). Stacks of confocal images were acquired using a Nikon Eclipse Ti microscope equipped with Plan Fluor 40×/1.3 and Plan Apo VC 60×/1.4 objectives and an A1R scanner using a pinhole of 1.2 airy units. Nucleolar areas were measured in 124 nucleoli for the WT worms and 146 nucleoli for the *baf-1(G12T)*, representing >20 animals per strain over 4 independent experiments, after creating binary masks with Fiji software from the original images (65).

C. elegans RNAi

For RNA interference, were fed with E. coli that express double-stranded RNA (dsRNA). Bacterial clones were obtained from a genome wide RNAi library (66) except clones corresponding to *mel-28, npp-6, npp-20, rpn-9* and *rpl-13* that were obtained from alternative sources (67-69). RNAi plasmids for *csk-1, daf-4, gft-2H3, src-1, ced-9* and *mrpl-36* were constructed as described (70) using the PCR primers listed in Supplementary Table 2. PCR fragments were inserted into plasmid pL4440 npp-15 (68) after digestion with XhoI (NEB R0146S) and SpeI (NEB R3133S), ligation and subsequent transformation into E. coli DH5α. Plasmids from ampicillin resistant colonies were confirmed by restriction digestion, transformed into E. coli HT115 and plated on LB with ampicillin and tetracycline. For RNAi experiments, 12-15 homozygous yc32[gfp::lmn-1]; baf-1(bq19[G12T]) hermaphrodites were

transferred at L4 stage to RNAi plates containing dsRNA-producing E. coli HT115, 1 mM IPTG and 100 µg/ml ampicillin and incubated at 20°C. After 18 hours, 1-day old adults were transferred to fresh RNAi plates (3 animals per plate; nine worms in total per replica) and incubated for 6 hours at 20°C. The adults were then removed and rescue of lethality was determined by counting the number of unhatched embryos and viable offspring after 24 hours at 20°C.

Statistical analysis of *C. elegans* data

Data were analyzed in R Studio (1.3.1093 (71); running R 4.0.2 (72)) and represented with base plotting. Mann-Whitney and t-tests were performed in R Studio and adjusted for multiple comparison (Benjamini & Hochberg method) when relevant. *C. elegans* has two sexes: hermaphrodites and males. The viability experiments reported in this manuscript can only be performed with hermaphrodites. There is therefore no sex specific analysis performed.

Data availability: The RNA Seq data has been deposited on GEO with the accession number GSE269484 [https://www.ncbi.nlm.nih.gov/geo/query/acc.cgi?acc=GSE269484].

eQTL data from the eQTLGen study was accessed using the Phase I release of cis-eQTLs and is available for download via https://eqtlgen.org/phase1.html. GWAS summary statistics are available via https://zenodo.org/records/1251813 from the GIANT consortium, via https://csg.sph.umich.edu/willer/public/glgc-lipids2021/ from the GLGC consortium and via http://www.gefos.org/ from the GEFOS consortium. All other source data are provided with the paper.

REFERENCES

1. A. De Sandre-Giovannoli *et al.*, Lamin a truncation in Hutchinson-Gilford progeria. *Science* **300**, 2055 (2003).
2. M. Eriksson *et al.*, Recurrent de novo point mutations in lamin A cause Hutchinson-Gilford progeria syndrome. *Nature* **423**, 293-298 (2003).
3. R. Cabanillas *et al.*, Nestor-Guillermo progeria syndrome: a novel premature aging condition with early onset and chronic development caused by BANF1 mutations. *Am J Med Genet A* **155A**, 2617-2625 (2011).
4. X. S. Puente *et al.*, Exome sequencing and functional analysis identifies BANF1 mutation as the cause of a hereditary progeroid syndrome. *Am J Hum Genet* **88**, 650-656 (2011).
5. C. M. Bradley, D. R. Ronning, R. Ghirlando, R. Craigie, F. Dyda, Structural basis for DNA bridging by barrier-to-autointegration factor. *Nat Struct Mol Biol* **12**, 935-936 (2005).
6. R. Zheng *et al.*, Barrier-to-autointegration factor (BAF) bridges DNA in a discrete, higher-order nucleoprotein complex. *Proc Natl Acad Sci U S A* **97**, 8997-9002 (2000).
7. C. Samson *et al.*, Structural analysis of the ternary complex between lamin A/C, BAF and emerin identifies an interface disrupted in autosomal recessive progeroid diseases. *Nucleic Acids Res* **46**, 10460-10473 (2018).
8. M. Cai *et al.*, Solution NMR structure of the barrier-to-autointegration factor-Emerin complex. *J Biol Chem* **282**, 14525-14535 (2007).
9. T. Haraguchi *et al.*, BAF is required for emerin assembly into the reforming nuclear envelope. *J Cell Sci* **114**, 4575-4585 (2001).
10. M. Gorjanacz *et al.*, Caenorhabditis elegans BAF-1 and its kinase VRK-1 participate directly in post-mitotic nuclear envelope assembly. *EMBO J* **26**, 132-143 (2007).
11. A. M. Young, A. L. Gunn, E. M. Hatch, BAF facilitates interphase nuclear membrane repair through recruitment of nuclear transmembrane proteins. *Mol Biol Cell* **31**, 1551-1560 (2020).
12. L. B. Gordon, F. G. Rothman, C. Lopez-Otin, T. Misteli, Progeria: a paradigm for translational medicine. *Cell* **156**, 400-407 (2014).
13. M. A. Merideth *et al.*, Phenotype and course of Hutchinson-Gilford progeria syndrome. *N Engl J Med* **358**, 592-604 (2008).

14. A. Janssen *et al.*, The BAF A12T mutation disrupts lamin A/C interaction, impairing robust repair of nuclear envelope ruptures in Nestor-Guillermo progeria syndrome cells. *Nucleic Acids Res*, **50**, 9260-9278 (2022).
15. Y. Kono *et al.*, Nucleoplasmic Lamin C Rapidly Accumulates at Sites of Nuclear Envelope Rupture with BAF and cGAS. *bioRxiv*, 2022.2001.2005.475028 (2022).
16. R. M. Sears, K. J. Roux, Mechanisms of A-Type Lamin Targeting to Nuclear Ruptures Are Disrupted in LMNA- and BANF1-Associated Progerias. *Cells* **11**, (2022).
17. R. D. Goldman *et al.*, Accumulation of mutant lamin A causes progressive changes in nuclear architecture in Hutchinson-Gilford progeria syndrome. *Proc Natl Acad Sci U S A* **101**, 8963-8968 (2004).
18. B. Liu *et al.*, Genomic instability in laminopathy-based premature aging. *Nat Med* **11**, 780-785 (2005).
19. C. Lopez-Otin, M. A. Blasco, L. Partridge, M. Serrano, G. Kroemer, The hallmarks of aging. *Cell* **153**, 1194-1217 (2013).
20. P. Scaffidi, T. Misteli, Reversal of the cellular phenotype in the premature aging disease Hutchinson-Gilford progeria syndrome. *Nat Med* **11**, 440-445 (2005).
21. P. Taimen *et al.*, A progeria mutation reveals functions for lamin A in nuclear assembly, architecture, and chromosome organization. *Proc Natl Acad Sci U S A* **106**, 20788-20793 (2009).
22. S. Gonzalo, R. Kreienkamp, DNA repair defects and genome instability in Hutchinson-Gilford Progeria Syndrome. *Curr Opin Cell Biol* **34**, 75-83 (2015).
23. M. Loi *et al.*, Barrier-to-autointegration factor (BAF) involvement in prelamin A-related chromatin organization changes. *Oncotarget* **7**, 15662-15677 (2016).
24. D. Larrieu, S. Britton, M. Demir, R. Rodriguez, S. P. Jackson, Chemical inhibition of NAT10 corrects defects of laminopathic cells. *Science* **344**, 527-532 (2014).
25. G. Balmus *et al.*, Targeting of NAT10 enhances healthspan in a mouse model of human accelerated aging syndrome. *Nat Commun* **9**, 1700 (2018).
26. D. Larrieu *et al.*, Inhibition of the acetyltransferase NAT10 normalizes progeric and aging cells by rebalancing the Transportin-1 nuclear import pathway. *Sci Signal* **11**, (2018).
27. B. C. Capell *et al.*, Inhibiting farnesylation of progerin prevents the characteristic nuclear blebbing of Hutchinson-Gilford progeria syndrome. *Proc Natl Acad Sci U S A* **102**, 12879-12884 (2005).
28. C. M. Denais *et al.*, Nuclear envelope rupture and repair during cancer cell migration. *Science* **352**, 353-358 (2016).

29. E. M. Hatch, M. W. Hetzer, Nuclear envelope rupture is induced by actin-based nucleus confinement. *J Cell Biol* **215**, 27-36 (2016).

30. N. Y. Chen, P. H. Kim, L. G. Fong, S. G. Young, Nuclear membrane ruptures, cell death, and tissue damage in the setting of nuclear lamin deficiencies. *Nucleus* **11**, 237-249 (2020).

31. S. Liao, M. Tammaro, H. Yan, Enriching CRISPR-Cas9 targeted cells by co-targeting the HPRT gene. *Nucleic Acids Res* **43**, e134 (2015).

32. J. Nasser *et al.*, Genome-wide enhancer maps link risk variants to disease genes. *Nature* **593**, 238-243 (2021).

33. A. Buchwalter, M. W. Hetzer, Nucleolar expansion and elevated protein translation in premature aging. *Nat Commun* **8**, 328 (2017).

34. T. Matt *et al.*, Dissociation of antibacterial activity and aminoglycoside ototoxicity in the 4-monosubstituted 2-deoxystreptamine apramycin. *Proc Natl Acad Sci U S A* **109**, 10984-10989 (2012).

35. R. Romero-Buono *et al*., A human progeria-associated BAF-1 mutation modulates gene expression and accelerates aging in *C. elegans*. *EMBO J. 2024 Oct 4.* doi: 10.1038/s44318-024-00261-8.

36. S. Ye *et al.*, LIS1 regulates osteoclast formation and function through its interactions with dynein/dynactin and Plekhm1. *PLoS One* **6**, e27285 (2011).

37. L. Wartosch, U. Gunesdogan, S. C. Graham, J. P. Luzio, Recruitment of VPS33A to HOPS by VPS16 Is Required for Lysosome Fusion with Endosomes and Autophagosomes. *Traffic* **16**, 727-742 (2015).

38. C. A. Spike, J. E. Shaw, R. K. Herman, Analysis of smu-1, a gene that regulates the alternative splicing of unc-52 pre-mRNA in Caenorhabditis elegans. *Mol Cell Biol* **21**, 4985-4995 (2001).

39. P. Papasaikas, J. R. Tejedor, L. Vigevani, J. Valcarcel, Functional splicing network reveals extensive regulatory potential of the core spliceosomal machinery. *Mol Cell* **57**, 7-22 (2015).

40. N. Kubben *et al.*, Repression of the Antioxidant NRF2 Pathway in Premature Aging. *Cell* **165**, 1361-1374 (2016).

41. P. Jevtic *et al.*, The nucleoporin ELYS regulates nuclear size by controlling NPC number and nuclear import capacity. *EMBO Rep* **20**, e47283 (2019).

42. W. R. Xing, H. Goodluck, C. Zeng, S. Mohan, Role and mechanism of action of leucine-rich repeat kinase 1 in bone. *Bone Res* **5**, 17003 (2017).

43. M. Si *et al.*, LRRK1 regulation of actin assembly in osteoclasts involves serine 5 phosphorylation of L-plastin. *J Cell Biochem* **119**, 10351-10357 (2018).

44. C. Zeng *et al.*, Leucine-rich repeat kinase-1 regulates osteoclast function by modulating RAC1/Cdc42 Small GTPase phosphorylation and activation. *Am J Physiol Endocrinol Metab* **311**, E772-E780 (2016).

45. W. Xing *et al.*, Targeted disruption of leucine-rich repeat kinase 1 but not leucine-rich repeat kinase 2 in mice causes severe osteopetrosis. *J Bone Miner Res* **28**, 1962-1974 (2013).

46. C. Kenyon, The plasticity of aging: insights from long-lived mutants. *Cell* **120**, 449-60 (2005).

47. P. Zhu *et al*., Correlated evolution of social organization and lifespan in mammals. *Nat Commun* **14**, 372 (2023).

48. S. Zhang *et al*., *Caenorhabditis elegans* as a Useful Model for Studying Aging Mutations. *Front Endocrinol (Lausanne)* **11**, 554994 (2020). 49. K. Z. Pan *et al.*, Inhibition of mRNA translation extends lifespan in Caenorhabditis elegans. *Aging Cell* **6**, 111-119 (2007).

50. M. Hansen *et al.*, Lifespan extension by conditions that inhibit translation in Caenorhabditis elegans. *Aging Cell* **6**, 95-110 (2007).

51. T. Jimenez-Saucedo, J. J. Berlanga, M. Rodriguez-Gabriel, Translational control of gene expression by eIF2 modulates proteostasis and extends lifespan. *Aging (Albany NY)* **13**, 10989-11009 (2021).

52. D. Shcherbakov *et al.*, Premature aging in mice with error-prone protein synthesis. *Sci Adv* **8**, eabl9051 (2022).

53. A. F. J. Janssen, S. Y. Breusegem, D. Larrieu, Current Methods and Pipelines for Image-Based Quantitation of Nuclear Shape and Nuclear Envelope Abnormalities. *Cells* **11**, (2022).

54. E. Becht *et al.*, Dimensionality reduction for visualizing single-cell data using UMAP. *Nat Biotechnol*, (2018).

55. S. L. Pulit *et al.*, Meta-analysis of genome-wide association studies for body fat distribution in 694 649 individuals of European ancestry. *Hum Mol Genet* **28**, 166-174 (2019).

56. S. E. Graham *et al.*, The power of genetic diversity in genome-wide association studies of lipids. *Nature* **600**, 675-679 (2021).

57. J. A. Morris *et al.*, An atlas of genetic influences on osteoporosis in humans and mice. *Nat Genet* **51**, 258-266 (2019).

58. Z. Zhu *et al.*, Integration of summary data from GWAS and eQTL studies predicts complex trait gene targets. *Nat Genet* **48**, 481-487 (2016).

59. U. Vosa *et al.*, Large-scale cis- and trans-eQTL analyses identify thousands of genetic loci and polygenic scores that regulate blood gene expression. *Nat Genet* **53**, 1300-1310 (2021).

60. C. A. de Leeuw, J. M. Mooij, T. Heskes, D. Posthuma, MAGMA: generalized gene-set analysis of GWAS data. *PLoS Comput Biol* **11**, e1004219 (2015).

61. C. R. Bone, Y. T. Chang, N. E. Cain, S. P. Murphy, D. A. Starr, Nuclei migrate through constricted spaces using microtubule motors and actin networks in C. elegans hypodermal cells. *Development* **143**, 4193-4202 (2016).

62. A. K. Allen, J. E. Nesmith, A. Golden, An RNAi-based suppressor screen identifies interactors of the Myt1 ortholog of Caenorhabditis elegans. *G3 (Bethesda)* **4**, 2329-2343 (2014).

63. T. Stiernagle, Maintenance of C. elegans. *WormBook*, 1-11 (2006).

64. P. de la Cruz Ruiz, R. Romero-Bueno, P. Askjaer, Analysis of Nuclear Pore Complexes in Caenorhabditis elegans by Live Imaging and Functional Genomics. *Methods Mol Biol* **2502**, 161-182 (2022).

65. J. Schindelin *et al.*, Fiji: an open-source platform for biological-image analysis. *Nat Methods* **9**, 676-682 (2012).

66. R. S. Kamath *et al.*, Systematic functional analysis of the Caenorhabditis elegans genome using RNAi. *Nature* **421**, 231-237 (2003).

67. J. F. Rual *et al.*, Toward improving Caenorhabditis elegans phenome mapping with an ORFeome-based RNAi library. *Genome Res* **14**, 2162-2168 (2004).

68. V. Galy, I. W. Mattaj, P. Askjaer, Caenorhabditis elegans nucleoporins Nup93 and Nup205 determine the limit of nuclear pore complex size exclusion in vivo. *Mol Biol Cell* **14**, 5104-5115 (2003).

69. V. Galy, P. Askjaer, C. Franz, C. Lopez-Iglesias, I. W. Mattaj, MEL-28, a novel nuclear-envelope and kinetochore protein essential for zygotic nuclear-envelope assembly in C. elegans. *Curr Biol* **16**, 1748-1756 (2006).

70. P. Askjaer, S. Ercan, P. Meister, Modern techniques for the analysis of chromatin and nuclear organization in C. elegans. *WormBook*, 1-35 (2014).

71. R. Team. (2020), pp. RStudio, PBC.

72. R. C. Team. (2020), pp. R Foundation for Statistical Computing.

Acknowledgments: We would like to thank Prof. Lopez Otin for providing us with the NGPS and WT immortalized fibroblasts, Dr Daniel Starr for providing us with the *gfp::lmn-1* alleles, Dr Dimitri Shcherbakov and Dr Erik Böttger for sharing the dual luciferase mistranslation assay plasmids. We thank Dr Dimitri Shcherbakov and Dr Mark Stoneley for helpful discussions on setting up and interpreting the assays, Matthew Gratian (CIMR microscopy) for his help with the high content microscope and screen set up, Henri Huppert (ThermoFisher) for his help with the HCS studio pipelines and Dr Gabriel Balmus for giving us access to the CyBio Felix robot. Funding: Sir Henry Dale Fellowship jointly funded by the Wellcome Trust and the Royal Society 206242/Z/17/Z (S.Y.B., D.L.). Wellcome Trust Institutional Strategic Support Fund 204845/Z/16/Z (A.F.J.J., D.L.). FEBS Long-Term Fellowship (A.F.J.J.). Spanish State Research Agency Grants PID2022-137162NB-I00 and CEX2020-001088-M (P.A.). Spanish State Research Agency Fellowship BES-2017-080216 (R.R.B.). Medical Research Council (Unit programs: MC_UU_12015/2, MC_UU_00006/2 (J. P., K.K.). Medical Research Council (MRC) [research grants MR/M010007/1 and MR/R0009015/1 to N.A.B. Swedish Research Council (VR) (2017-06088 and 2019-04868), the Swedish Cancer Society (Cancerfonden) (20 1034 Pj and 23 2994 Pj), and the Novo Nordisk Foundation (NNF21OC0070427 and NNF22OC0078353) to C.G.R.

Author contributions:

Conceptualization: DL

Methodology: SYB, JH, AFJJ, AFL, RRB, CGR, KK, NAB, KKO, JRBP, DL

Investigation: SYB, JH, AFJJ, AFL, RRB, KK, NAB, DL

Visualization: SYB, AFJJ, AFL, RRB, KK, NAB, PA, DL

947 Funding acquisition: DL, PA, JRBP, KKO

948 Project administration: DL

949 Supervision: DL, PA, JRBP, KKO

950 Writing – original draft: DL, SYB

951 Writing – review & editing: SYB, DL, JH, AFJJ, KK, JRBP, PA, NAB, KKO

952 All authors have approved the final version of this manuscript.

953

954 **Competing interests:** D. L. is an employee of Altos Labs. JRBP is an employee/shareholder
955 of Insmed. J.R.B.P. also receives research funding from GSK and consultancy fees from WW
956 International. The other authors declare that they have no competing interests.

957

FIGURE LEGENDS

Fig. 1. NGPS fibroblasts show distinctive phenotypes to HGPS. (**A**) Representative transmission electron micrographs of WT, NGPS1 and NGPS2 fibroblasts (males). (**B**) Representative high resolution microscopy images showing the expression and localization of lamin B1 and emerin in WT and NGPS fibroblasts. (**C**) Immunofluorescence images showing DNA damage foci (53BP1) and nucleocytoplasmic transport (Ran) in WT and NGPS fibroblasts. Images were obtained with the CX7 high-content microscope and quantified in (**D**) and (**E**) using the HCS Studio^{TM} software. (**D**): Superplot of the data (3 technical replicates in 3 independent experiments), lines indicate average values, statistical analysis using nested one-way ANOVA with Dunnett's multiple comparisons. (**E**): Data from 3 independent experiments, 2-3 technical replicates each, lines indicate average values, statistical comparison using one-way ANOVA with Dunnett's multiple comparisons. (**F**) High resolution microscopy images of the heterochromatin marker HP1γ in WT and NGPS cells. (**G**) Nuclear HP1γ levels quantified using the high-content microscope in 2 independent experiments, each averaging 500 nuclei in 3 wells. Means ± SD are shown. For the NGPS cells statistical testing used one-way ANOVA with Dunnett's multiple comparisons; HGPS cells were compared to WT using two-tailed unpaired t-test. (**H**) Representative Western blot and (**I**) quantitative analysis of 4 independent experiments showing HP1γ in NGPS cells compared to WT. (**J**-**L**) Representative western blots and quantitative analysis of 3 independent experiments, showing the heterochromatin marks H3K9me3 (**J**) and H3K79me2 (**K**) or the aging and senescence marker p21 (**L**) in NGPS cells compared to WT. In (**I**-**L**) data points are overlaid on columns indicating the mean +/- SD, and statistical analysis used one-way ANOVA with Dunnett's multiple comparisons.

Fig. 2. Whole genome CRISPR screening set-up in NGPS fibroblasts. (**A**) Schematic detailing the four main steps involved in the CRISPR screen set-up (Created in BioRender. Larrieu, D. (2024) BioRender.com/e32i842). (**B**) Example immunofluorescence images of the indicated stainings used in the screen and obtained with the high-content microscope. (**C**) Quantification of the nucleus to cytoplasmic (N:C) emerin intensity ratio in WT and NGPS2 cells. (**D**) Quantification of the nuclear shape in WT and NGPS2 cells using a perimeter to area (P2A) analysis obtained with HCS Studio. Each data point in (**C**) and (**D**) is the average value measured over 500 cells, in 7 independent experiments; lines indicate the average ± SD and unpaired two-tailed t-tests were used for statistical analysis. (**E**) Graphical representation and corresponding immunofluorescence images showing the identification of blebs as the origin of NE ruptures using a nuclear localization signal (NLS) reporter tagged with a GFP. (**F**, **G**) Representative nuclei imaged with the CX7 microscope, showing the outlines of the nuclei in blue, and the nuclear blebs (F) or micronuclei (G) in yellow as detected by the HCS software and quantified (as in C and D) in (**H** and **I**). Each data point in (**H**) and (**I**) is the average value measured over 500 cells, in 7 independent experiments; lines indicate the average ± SD and unpaired two-tailed t-tests were used for statistical analysis (**J**) Knock down efficiency of individual or pooled crRNAs assessed in the clonal population of Cas9-expressing WT and NGPS cells. crRNAs targeting SIRT7 (top 2 blots) or HDAC6 (bottom 3 blots) were used, either as single sequences (#1, #2) or as a pool of the 2 sequences. (**K**) Representative immunofluorescence images of emerin intensity in NGPS1-Cas9 cells upon transfection of a pool of 3 crRNAs or sgRNAs and quantified in 2 independent experiments using the HCS image studio software (right panel). (**L**) Comparison of cell growth inhibition upon transfection of the indicated sgRNA or crRNA in NGPS1-Cas9 cells. The growth rate was measured using an Incucyte S3 live-cell analysis system in 2 independent experiments. The

data shows the representative cell growth from 4 images/well, (average ± SD indicated by lines).

Fig. 3. Identification of genes and pathways modulating NGPS phenotypes. (**A**) Schematic showing the experimental outline of the primary and validation screens in NGPS2-Cas9 fibroblasts (Created in BioRender. Larrieu, D. (2024) BioRender.com/e32i842). (**B**) Uniform Manifold Approximation and Projection (UMAP) of the cluster analysis from the primary screen. Nuclear shape, micronuclei and NE blebs frequency quantified in NGPS2-Cas9 cells (grey dots) for each single knock-out were reduced to two dimensions and mapped alongside the same parameters measured in matching control cells (blue dots). The hit genes are labeled in red. (**C**-**F**) S plots depicting the top 20 genes with the highest and lowest Z scores for each individual phenotype quantified from the NGPS genome-wide CRISPR screen alongside the mean value obtained for the NGPS cells (red bars) and the wild type cells (black bars) transfected with a non-targeting crRNA.

Fig. 4: Validation of hits normalizing multiple nuclear envelope phenotypes in NGPS cells. (**A-B**) Biological processes gene set enrichment was carried out using the clusterProfiler R package. P values were calculated through clusterProfiling using a hypergeometric distribution which corresponds to a one-sided version of Fisher's exact test. No corrections for multiple comparisons were applied. The 43 validated genes were tested against a full homo sapiens ontology database. (**C**) Representative immunofluorescence images obtained in the validation screen, showing the effects of some of the hits on the nuclear envelope phenotypes. (**D**) Heatmap showing the overlap between identified target genes and human genetic datasets. For all four phenotypic traits (BMI (n= 806,834), WHR (n=694,649), triglycerides (n=1,253,275) and eBMD, (n=426,824)), target genes were annotated on the basis of (i) proximity to GWAS signals, (ii) coding-variant gene-level associations to the trait (MAGMA), (iii) colocalization between the GWAS and eQTL data and (iv) the presence of known enhancers within the association peaks. A count of the observed concordant predictors (out of a maximum of 16) is displayed in Summary (right panel). Expanded results can be found in Supplementary Data 8.

Fig. 5. BAF A12T is associated with enhanced protein synthesis and translation errors. (**A-B**) Differential gene expression analysis in wild-type compared to NGPS1 and NGPS2 cell lines reveals enrichment for biological processes associated with RNA processing and translation. P-values were adjusted for multiple testing via the False Discovery Rate (FDR; Benjamini-Hochberg) approach. Gene Ontology Analysis was performed on genes with a False Discovery Rate value less than 0.01. (**C**) Nascent protein synthesis assay using HPG incorporation followed by labelling using a "click" reaction with Alexa fluor 488 (AF 488) in WT, NGPS2 or NGPS2 corrected (**C**) or in WT fibroblasts expressing a BAF WT or BAF A12T construct (**D**). AF 488-HPG intensity was quantified using the high-content microscope in 4 (**C**) or 3 (**D**) independent experiments, each measuring 1000 cells in 3 wells per cell line, graphed as a Superplot with data from different experiments indicated in different colors and larger symbols indicating each experiment's average. AF 488-HPG intensity was normalized to the WT cell line. Mean values were analyzed using nested one-way ANOVA (**C**) or paired two-tailed t-test (**D**), with Tukey's method used for multiple comparisons in (**C**). (**E**) Immunofluorescence images of nucleolin used to identify and outline the nucleoli (yellow) in the indicated cell lines using the HCS Studio software. (**F-G**) Average nucleolar area quantified in NGPS2 and NGPS2 corrected cells (**F**) or in WT fibroblasts expressing BAF WT or BAF A12T (**G**). (**F**) and (**G**) are superplots as in (**C-D**), and statistical comparisons were made using paired two-tailed t-tests. (**H**) Translation error rate measured as an increased read-through using a dual luciferase assay in 3 independent repeats (Superplot of the data). Mean values were analyzed using one-way ANOVA with Dunnett's multiple comparison testing. Results are derived from the ratio hFluc/hRluc, given in fold induction.

Fig. 6. Inhibition of protein synthesis restores nuclear envelope abnormalities in NGPS cells. (**A**) Nascent protein synthesis assay based on fluorescence intensity of HPG AF 488. NGPS2 or NGPS2 corrected cells (NGPS WT) were imaged with the high throughput microscope following siRNA depletion of 41 of the validated screen hits. Depletion of genes highlighted in blue show significant (one-way ANOVA with Dunnett's multiple comparisons test, $p<0.05$) reduction of HPG incorporation compared to NGPS2 cells transfected with a non-targeting siRNA (red dotted line). Shown are averages ± SD of 3 independent experiments in 500 cells. (**B**) Quantification of emerin nuclear intensity in NGPS1 and NGPS2 cell lines compared to WT, upon protein synthesis inhibition using cycloheximide (CHX) or silvestrol. Superplots of the 3 independent experiments are shown, and nested one-way ANOVA was used for statistical comparisons with Dunnett's multiple comparison testing. (**C**) Representative immunofluorescence images of emerin staining upon protein synthesis inhibition by treatment with CHX or silvestrol.

Fig. 7. Depletion of PAFAH1B1, RPS3A, SMU1 and VPS16 suppress the larvae lethality of an NGPS hermaphrodite *C. elegans* model. (A) Confocal images of hypodermal nuclei of live wild-type (WT; strain COP262) and NGPS (G12T; strain BN1389) 1 day old adult hermaphrodites *C. elegans* expressing FIB-1::GFP. Shown are overlays of GFP (green) and DIC images. Scale bar 5 um. **(B)** Nucleolar area was measured in 124 nucleoli for the WT worms and 146 nucleoli for the *baf-1(G12T)*, representing >20 animals per strain over 4 independent experiments. Black lines show the average nucleolar area ± SD. The p-value from Welch two sample t-test is indicated. **(C)** The indicated genes were knocked down by RNAi and tested for suppression of lethality in *gfp::lmn-1, baf-1(G12T)* hermaphrodites (strain BN1336). Each point corresponds to the percentage of eggs developing into larvae from a single plate with 50-100 eggs laid by 1 day old adult hermaphrodites. For PAFAH1B1, 9 plates were analysed for both the control and PAFAH1B1, over 3 independent experiments. For RPS3A, 15 control plates and 14 RPS3A plates were analysed over 4 independent experiments. For SMU1, 14 control and 16 SMU-1 plates were analysed over 5 independent experiments. For VPS16, 12 controls and 11 VPS16 plates were analysed over 4 independent experiments. Black lines indicate medians. Mann-Whitney test p-values were calculated for each set of control and test plates.

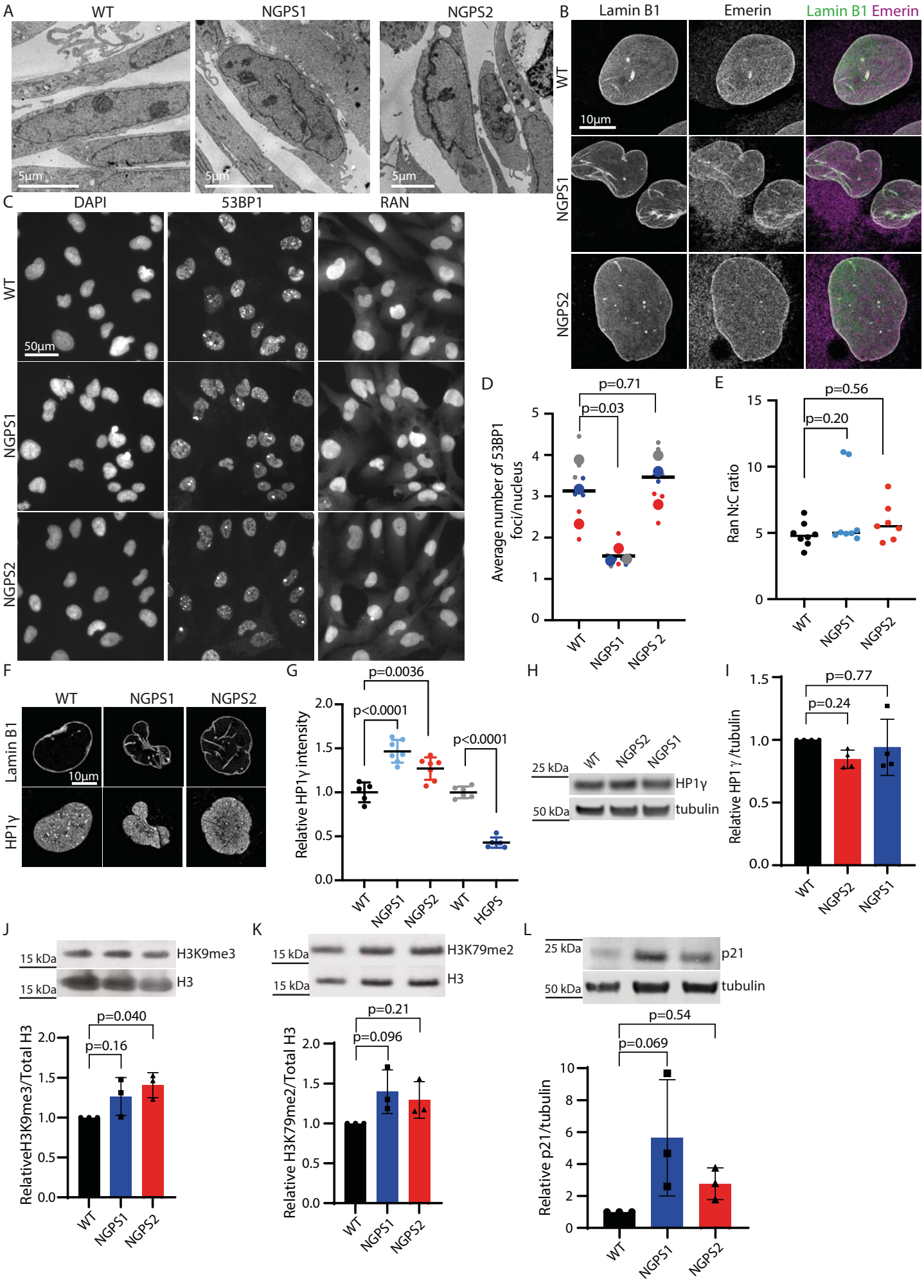
A
WT
NGPS1
NGPS2
5µm
B
Lamin B1
Emerin
Lamin B1 Emerin
WT
NGPS1
NGPS2
10µm
C
DAPI
53BP1
RAN
50µm
D
Average number of 53BP1 foci/nucleus
p=0.71
p=0.03
E
Ran N:C ratio
p=0.56
p=0.20
F
Lamin B1
HP1γ
10µm
G
Relative HP1γ intensity
p=0.0036
p<0.0001
p<0.0001
WT
NGPS1
NGPS2
HGPS
H
25 kDa
50 kDa
HP1γ
tubulin
I
Relative HP1γ/tubulin
p=0.77
p=0.24
J
15 kDa
H3K9me3
H3
RelativeH3K9me3/Total H3
p=0.040
p=0.16
K
H3K79me2
H3
Relative H3K79me2/Total H3
p=0.21
p=0.096
L
p21
tubulin
Relative p21/tubulin
p=0.54
p=0.069

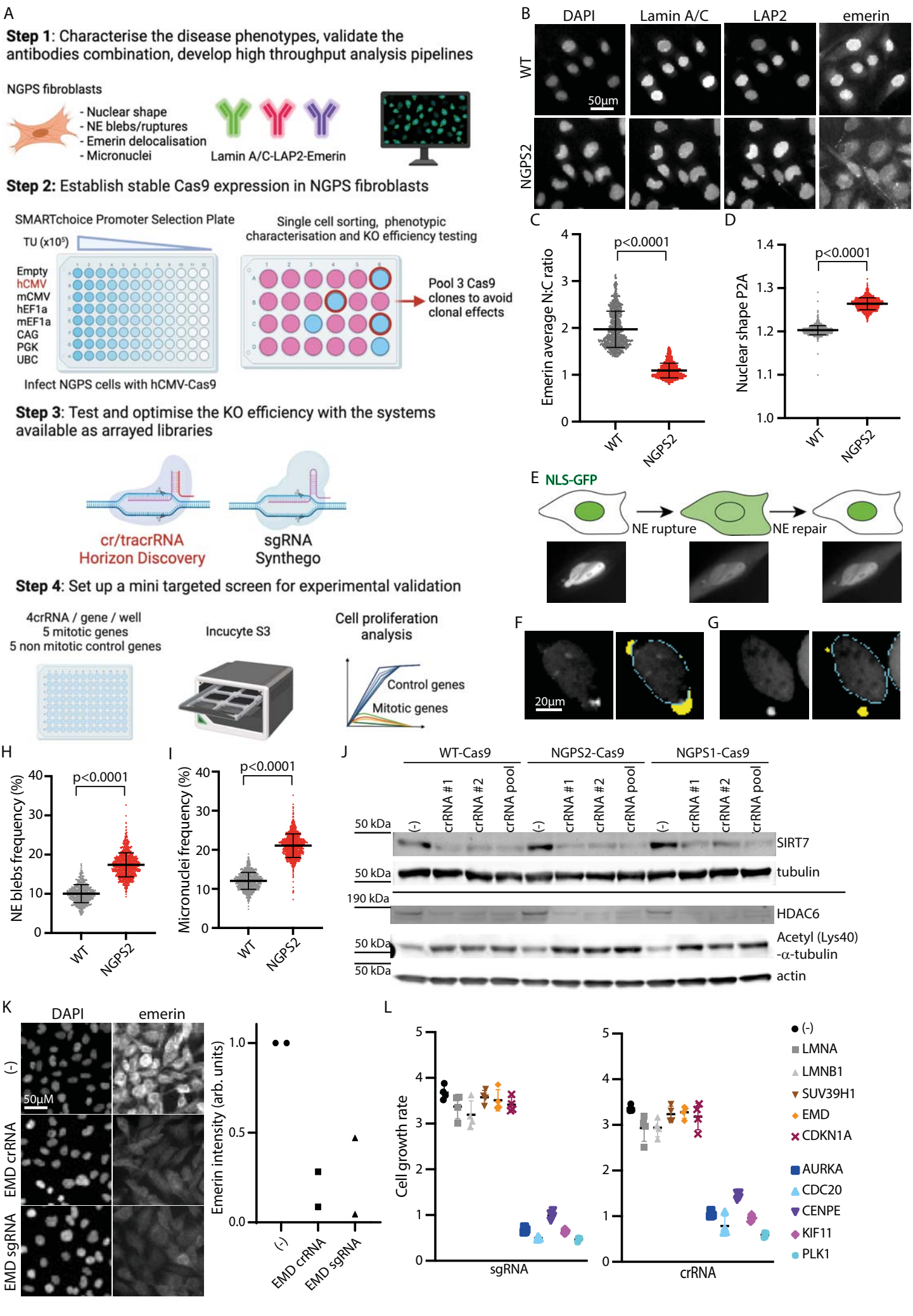
A
Step 1: Characterise the disease phenotypes, validate the antibodies combination, develop high throughput analysis pipelines
NGPS fibroblasts
- Nuclear shape
- NE blebs/ruptures
- Emerin delocalisation
- Micronuclei
Lamin A/C-LAP2-Emerin
Step 2: Establish stable Cas9 expression in NGPS fibroblasts
SMARTchoice Promoter Selection Plate
TU (x10⁵)
Empty
hCMV
mCMV
hEF1a
mEF1a
CAG
PGK
UBC
Infect NGPS cells with hCMV-Cas9
Single cell sorting, phenotypic characterisation and KO efficiency testing
Pool 3 Cas9 clones to avoid clonal effects
Step 3: Test and optimise the KO efficiency with the systems available as arrayed libraries
cr/tracrRNA
Horizon Discovery
sgRNA
Synthego
Step 4: Set up a mini targeted screen for experimental validation
4crRNA / gene / well
5 mitotic genes
5 non mitotic control genes
Incucyte S3
Cell proliferation analysis
Control genes
Mitotic genes
B
DAPI
Lamin A/C
LAP2
emerin
WT
NGPS2
50µm
C
Emerin average N:C ratio
p<0.0001
WT
NGPS2
D
Nuclear shape P2A
p<0.0001
WT
NGPS2
E
NLS-GFP
NE rupture
NE repair
F
20µm
G
H
NE blebs frequency (%)
p<0.0001
WT
NGPS2
I
Micronuclei frequency (%)
p<0.0001
WT
NGPS2
J
WT-Cas9
NGPS2-Cas9
NGPS1-Cas9
(-)
crRNA #1
crRNA #2
crRNA pool
50 kDa
SIRT7
tubulin
190 kDa
HDAC6
Acetyl (Lys40) -α-tubulin
actin
K
DAPI
emerin
(-)
EMD crRNA
EMD sgRNA
50µM
Emerin intensity (arb. units)
L
Cell growth rate
sgRNA
crRNA
(-)
LMNA
LMNB1
SUV39H1
EMD
CDKN1A
AURKA
CDC20
CENPE
KIF11
PLK1

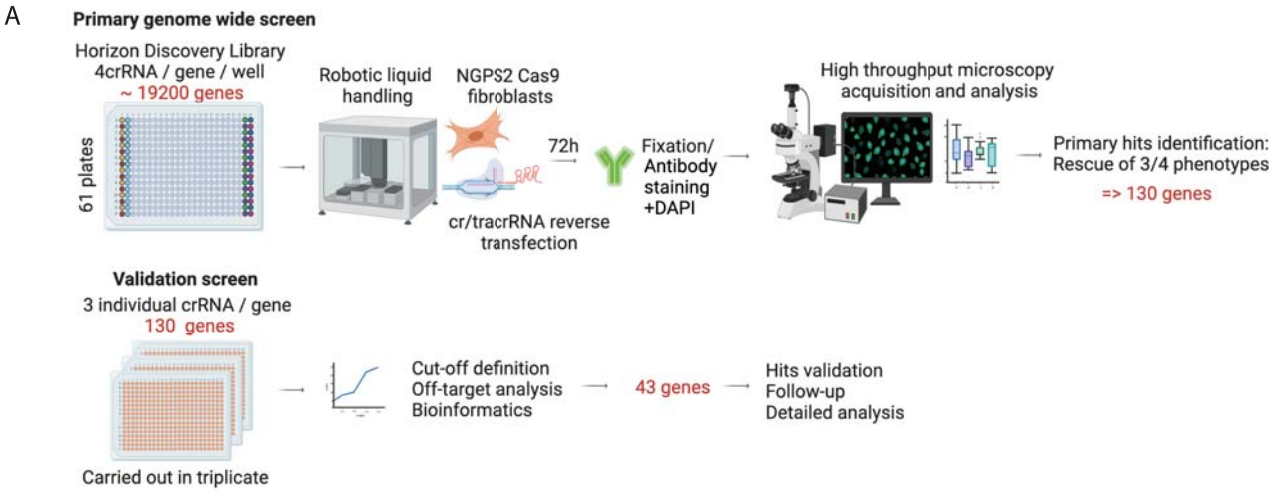
A
Primary genome wide screen
Horizon Discovery Library
4crRNA / gene / well
~ 19200 genes
61 plates
Robotic liquid handling
NGPS2 Cas9 fibroblasts
72h
cr/tracrRNA reverse transfection
Fixation/ Antibody staining +DAPI
High throughput microscopy acquisition and analysis
Primary hits identification: Rescue of 3/4 phenotypes
=> 130 genes
Validation screen
3 individual crRNA / gene
130 genes
Carried out in triplicate
Cut-off definition
Off-target analysis
Bioinformatics
43 genes
Hits validation
Follow-up
Detailed analysis

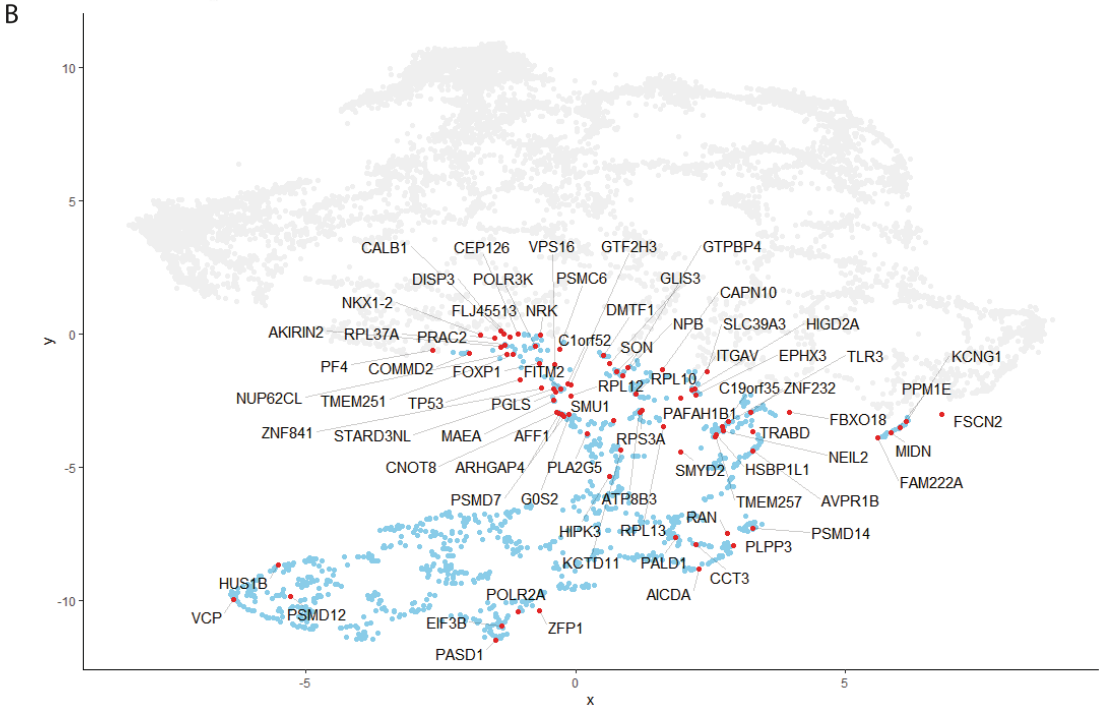
B
CALB1
CEP126
VPS16
GTF2H3
GTPBP4
DISP3
POLR3K
PSMC6
GLIS3
CAPN10
NKX1-2
FLJ45513
NRK
DMTF1
NPB
SLC39A3
HIGD2A
AKIRIN2
RPL37A
PRAC2
C1orf52
SON
ITGAV
EPHX3
TLR3
KCNG1
PF4
COMMD2
FOXP1
FITM2
RPL12
RPL10
C19orf35
ZNF232
PPM1E
NUP62CL
TMEM251
TP53
PGLS
SMU1
PAFAH1B1
FBXO18
FSCN2
ZNF841
STARD3NL
MAEA
AFF1
RPS3A
TRABD
NEIL2
MIDN
CNOT8
ARHGAP4
PLA2G5
SMYD2
HSBP1L1
FAM222A
PSMD7
G0S2
ATP8B3
TMEM257
AVPR1B
HIPK3
RPL13
RAN
PSMD14
PLPP3
KCTD11
PALD1
CCT3
HUS1B
AICDA
POLR2A
VCP
PSMD12
EIF3B
ZFP1
PASD1
x
y

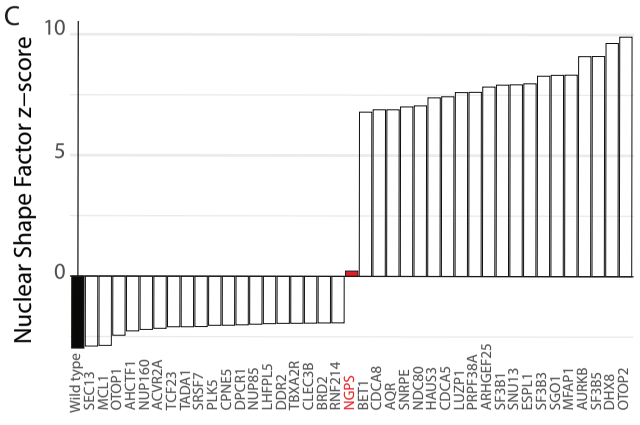
C
Nuclear Shape Factor z−score
Wild type
SEC13
MCL1
OTOP1
AHCTF1
NUP160
ACVR2A
TCF23
TADA1
SRSF7
PLK5
CPNE5
DPCR1
NUP85
LHFPL5
DDR2
TBXA2R
CLEC3B
BRD2
RNF214
NGPS
BET1
CDCA8
AQR
SNRPE
NDC80
HAUS3
CDCA5
LUZP1
PRPF38A
ARHGEF25
SF3B1
SNU13
ESPL1
SF3B3
SGOL1
MFAP1
AURKB
DHX8
OTOP2

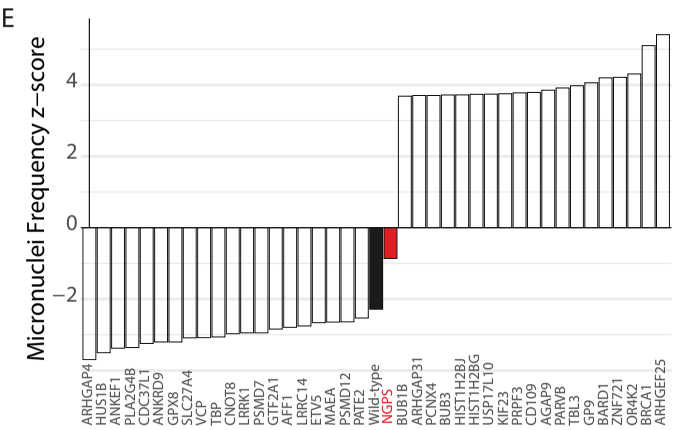
E
Micronuclei Frequency z−score
ARHGAP4
HUS1B
ANKEF1
PLA2G4B
CDC37L1
ANKRD9
GPX8
SLC27A4
VCP
TBP
CNOT8
LRRK1
PSMD7
GTF2A1
AFF1
LRRC14
ETV5
MAEA
PSMD12
PATE2
Wild-type
NGPS
BUB1B
ARHGAP31
PCNX4
BUB3
HIST1H2BJ
HIST1H2BG
USP17L10
KIF23
PRPF3
CD109
AGAP9
PARVB
TBL3
GP9
BARD1
ZNF721
OR4K2
BRCA1
ARHGEF25

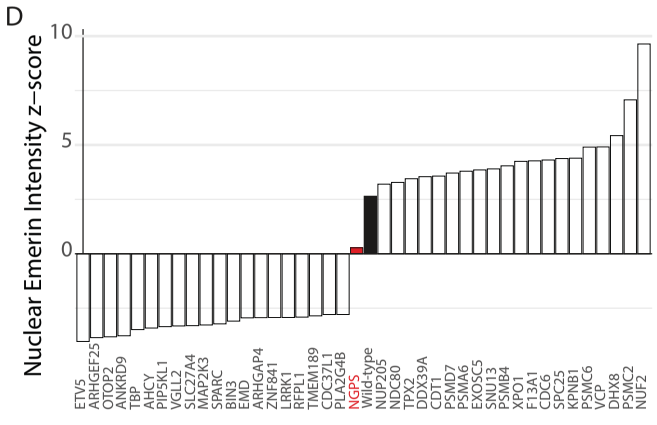
D
Nuclear Emerin Intensity z−score
ETV5
ARHGEF25
OTOP2
ANKRD9
TBP
AHCY
PIP5KL1
VGLL2
SLC27A4
MAP2K3
SPARC
BIN3
EMD
ARHGAP4
ZNF841
LRRK1
RFPL1
TMEM189
CDC37L1
PLA2G4B
NGPS
Wild-type
NUP205
NDC80
TPX2
DDX39A
CDT1
PSMD7
PSMA6
EXOSC5
SNU13
PSMB4
XPO1
F13A1
CDC6
SPC25
KPNB1
PSMC6
VCP
DHX8
PSMC2
NUF2

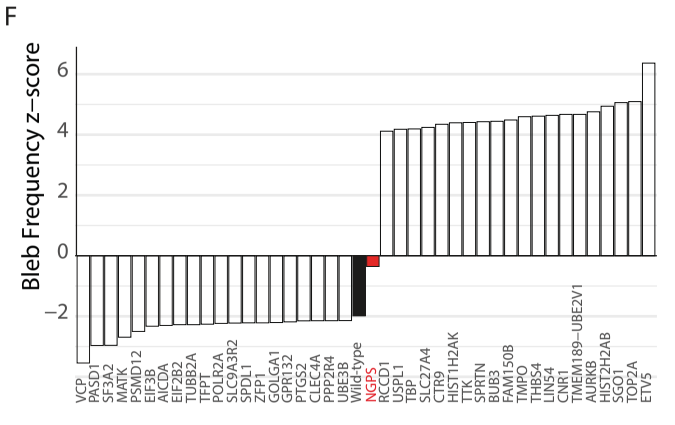
F
Bleb Frequency z−score
VCP
PASD1
SF3A2
MATK
PSMD12
EIF3B
AICDA
EIF2B2
TUBB2A
TFPT
POLR2A
SLC9A3R2
SPDL1
ZFP1
GOLGA1
GPR132
PTGS2
CLEC4A
PPP2R4
UBE3B
Wild-type
NGPS
RCCD1
ESPL1
TBP
SLC27A4
CTR9
HIST1H2AK
TTK
SPRTN
BUB3
FAM150B
TMPO
THBS4
LIN54
CNR1
TMEM189−UBE2V1
AURKB
HIST2H2AB
SGO1
TOP2A
ETV5

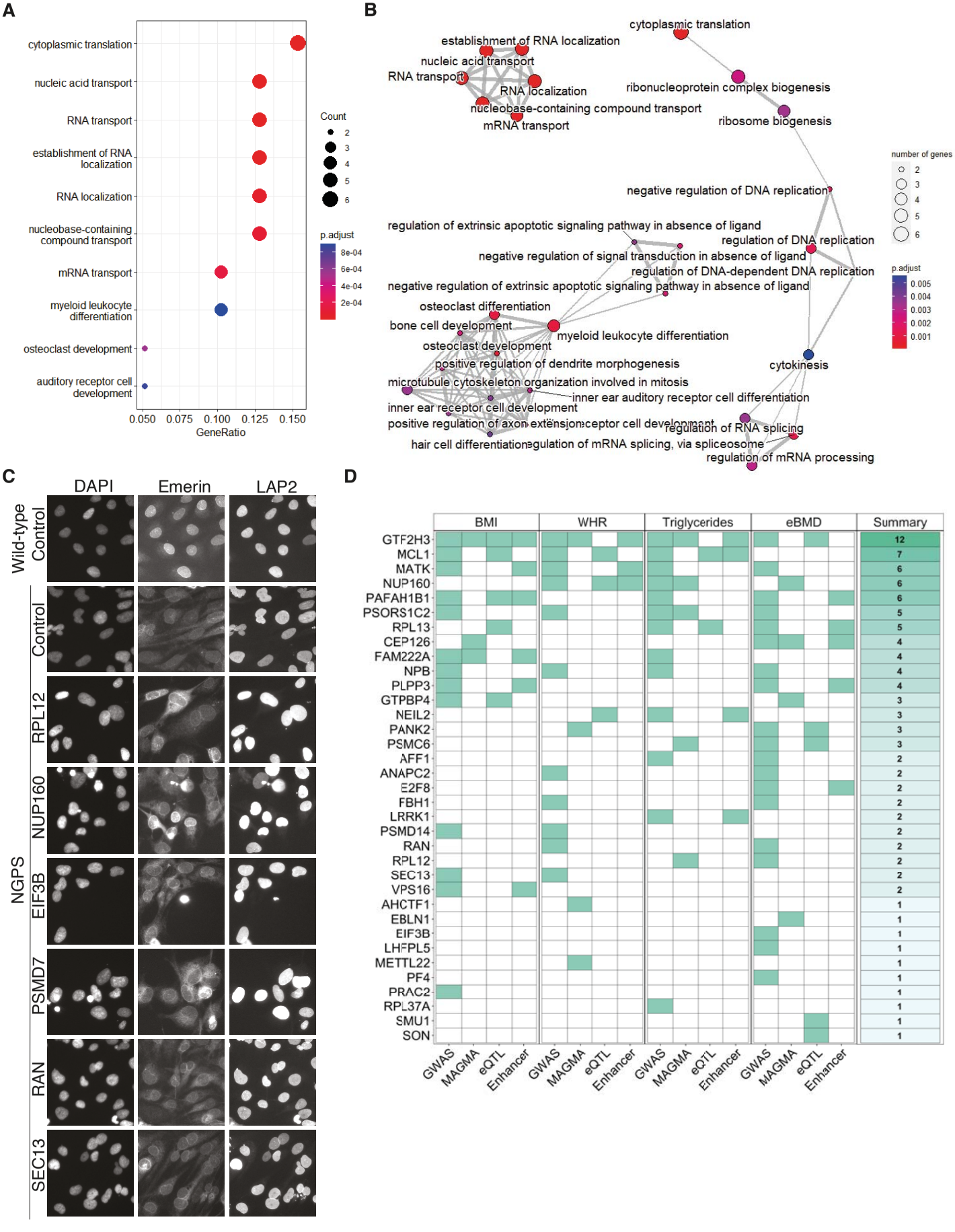
A
cytoplasmic translation
nucleic acid transport
RNA transport
establishment of RNA localization
RNA localization
nucleobase-containing compound transport
mRNA transport
myeloid leukocyte differentiation
osteoclast development
auditory receptor cell development
0.050 0.075 0.100 0.125 0.150
GeneRatio
Count
2 3 4 5 6
p.adjust
8e-04 6e-04 4e-04 2e-04
B
cytoplasmic translation
establishment of RNA localization
nucleic acid transport
RNA transport
RNA localization
nucleobase-containing compound transport
mRNA transport
ribonucleoprotein complex biogenesis
ribosome biogenesis
negative regulation of DNA replication
regulation of extrinsic apoptotic signaling pathway in absence of ligand
regulation of DNA replication
negative regulation of signal transduction in absence of ligand
regulation of DNA-dependent DNA replication
negative regulation of extrinsic apoptotic signaling pathway in absence of ligand
osteoclast differentiation
bone cell development
myeloid leukocyte differentiation
osteoclast development
positive regulation of dendrite morphogenesis
cytokinesis
microtubule cytoskeleton organization involved in mitosis
inner ear auditory receptor cell differentiation
inner ear receptor cell development
positive regulation of axon extension
ceptor cell development
regulation of RNA splicing
hair cell differentiation
egulation of mRNA splicing, via spliceosome
regulation of mRNA processing
number of genes
2 3 4 5 6
p.adjust
0.005 0.004 0.003 0.002 0.001
C
DAPI
Emerin
LAP2
Wild-type Control
NGPS
Control
RPL12
NUP160
EIF3B
PSMD7
RAN
SEC13
D
BMI
WHR
Triglycerides
eBMD
Summary
GTF2H3 12
MCL1 7
MATK 6
NUP160 6
PAFAH1B1 6
PSORS1C2 5
RPL13 5
CEP126 4
FAM222A 4
NPB 4
PLPP3 4
GTPBP4 3
NEIL2 3
PANK2 3
PSMC6 3
AFF1 2
ANAPC2 2
E2F8 2
FBH1 2
LRRK1 2
PSMD14 2
RAN 2
RPL12 2
SEC13 2
VPS16 2
AHCTF1 1
EBLN1 1
EIF3B 1
LHFPL5 1
METTL22 1
PF4 1
PRAC2 1
RPL37A 1
SMU1 1
SON 1
GWAS MAGMA eQTL Enhancer

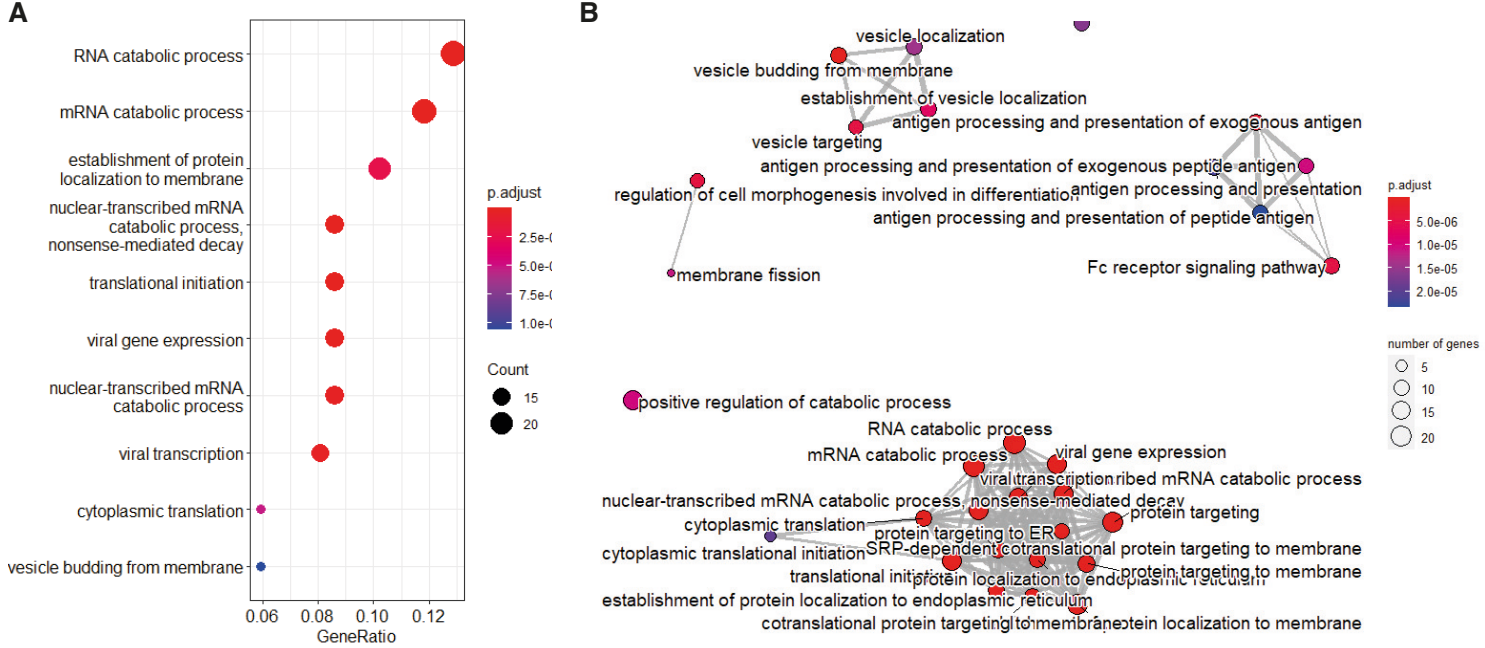
A
RNA catabolic process
mRNA catabolic process
establishment of protein localization to membrane
nuclear-transcribed mRNA catabolic process, nonsense-mediated decay
translational initiation
viral gene expression
nuclear-transcribed mRNA catabolic process
viral transcription
cytoplasmic translation
vesicle budding from membrane
0.06
0.08
0.10
0.12
GeneRatio
p.adjust
Count
15
20
B
vesicle localization
vesicle budding from membrane
establishment of vesicle localization
vesicle targeting
antigen processing and presentation of exogenous antigen
antigen processing and presentation of exogenous peptide antigen
antigen processing and presentation
antigen processing and presentation of peptide antigen
regulation of cell morphogenesis involved in differentiation
membrane fission
Fc receptor signaling pathway
p.adjust
5.0e-06
1.0e-05
1.5e-05
2.0e-05
number of genes
5
10
15
20
positive regulation of catabolic process
RNA catabolic process
mRNA catabolic process
viral gene expression
viral transcription
nuclear-transcribed mRNA catabolic process
nonsense-mediated decay
protein targeting
cytoplasmic translation
protein targeting to ER
cytoplasmic translational initiation
SRP-dependent cotranslational protein targeting to membrane
translational initiation
protein targeting to membrane
establishment of protein localization to endoplasmic reticulum
cotranslational protein targeting to membrane
protein localization to membrane

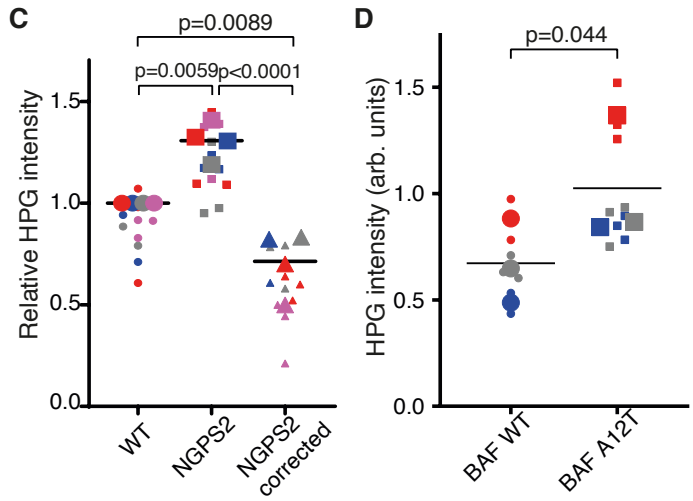
C
p=0.0089
p=0.0059
p<0.0001
Relative HPG intensity
1.5
1.0
0.5
0.0
WT
NGPS2
NGPS2 corrected

D
p=0.044
HPG intensity (arb. units)
1.5
1.0
0.5
0.0
BAF WT
BAF A12T

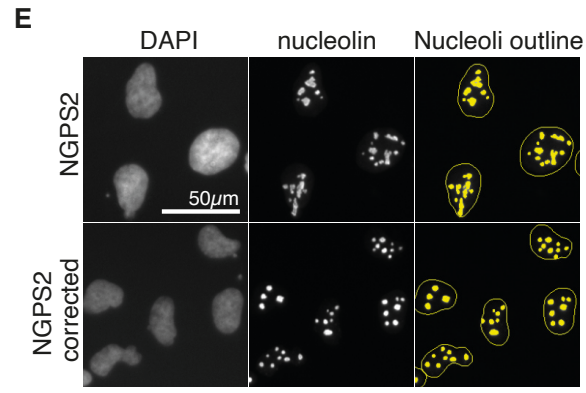
E
DAPI
nucleolin
Nucleoli outline
NGPS2
NGPS2 corrected
50μm

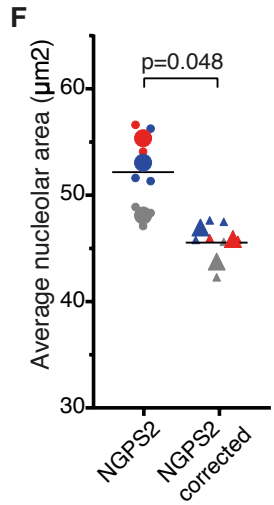
F
p=0.048
Average nucleolar area (μm2)
60
50
40
30
NGPS2
NGPS2 corrected

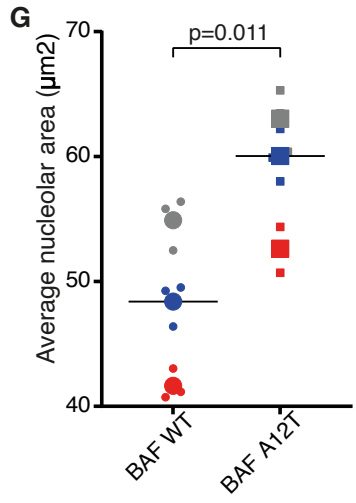
G
p=0.011
Average nucleolar area (μm2)
70
60
50
40
BAF WT
BAF A12T

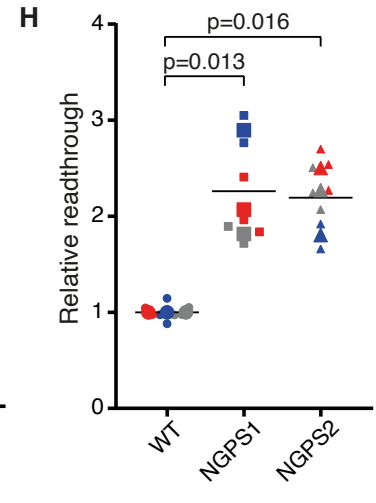
H
p=0.016
p=0.013
Relative readthrough
4
3
2
1
0
WT
NGPS1
NGPS2

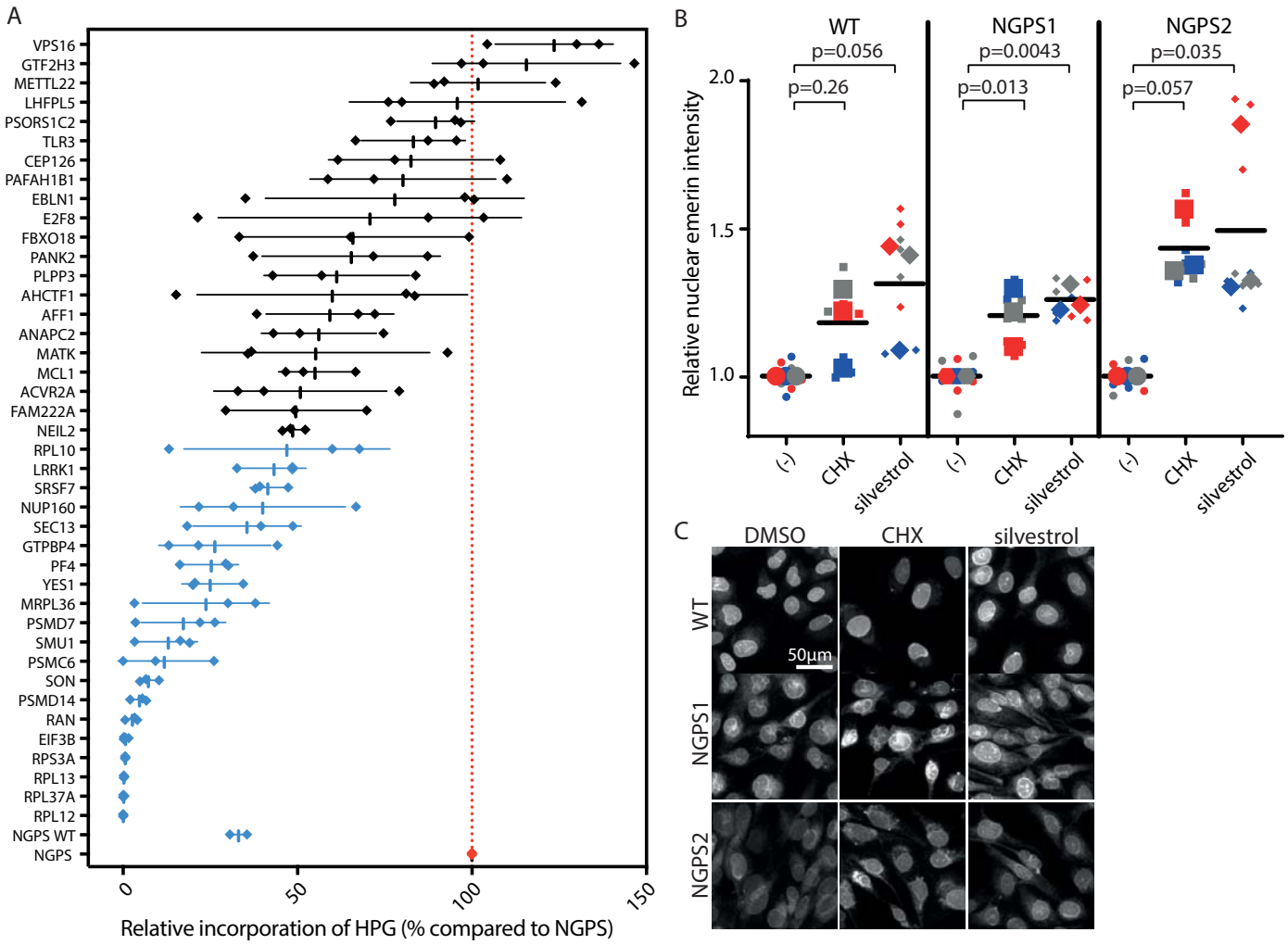
A
VPS16
GTF2H3
METTL22
LHFPL5
PSORS1C2
TLR3
CEP126
PAFAH1B1
EBLN1
E2F8
FBXO18
PANK2
PLPP3
AHCTF1
AFF1
ANAPC2
MATK
MCL1
ACVR2A
FAM222A
NEIL2
RPL10
LRRK1
SRSF7
NUP160
SEC13
GTPBP4
PF4
YES1
MRPL36
PSMD7
SMU1
PSMC6
SON
PSMD14
RAN
EIF3B
RPS3A
RPL13
RPL37A
RPL12
NGPS WT
NGPS
0
50
100
150
Relative incorporation of HPG (% compared to NGPS)
B
WT
NGPS1
NGPS2
p=0.056
p=0.26
p=0.0043
p=0.013
p=0.035
p=0.057
Relative nuclear emerin intensity
2.0
1.5
1.0
(-)
CHX
silvestrol
C
DMSO
CHX
silvestrol
WT
NGPS1
NGPS2
50µm

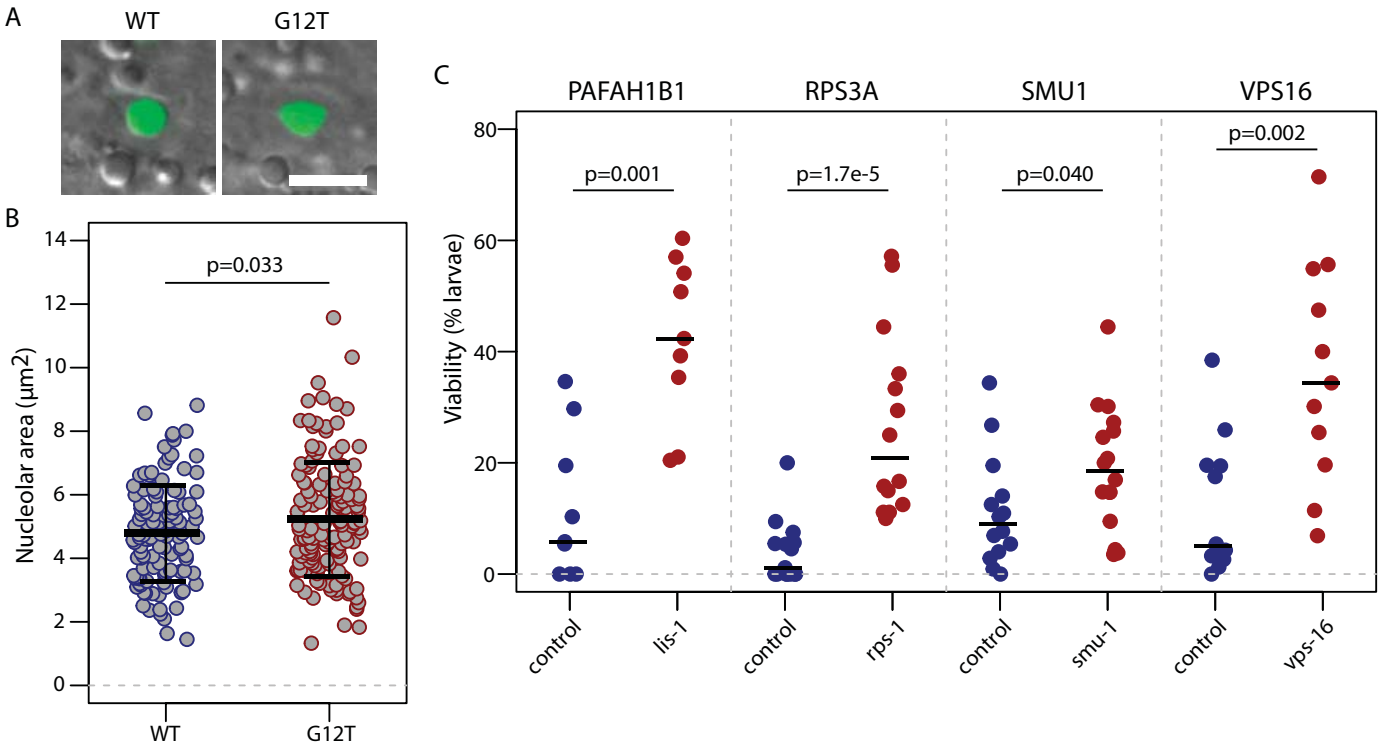
A
WT
G12T
B
p=0.033
Nucleolar area (µm2)
14
12
10
8
6
4
2
0
WT
G12T
C
PAFAH1B1
RPS3A
SMU1
VPS16
p=0.001
p=1.7e-5
p=0.040
p=0.002
Viability (% larvae)
80
60
40
20
0
control
lis-1
control
rps-1
control
smu-1
control
vps-16